

with an indent measuring digital eyepiece device was used to quantify specimen hardness, connected to an automatic counter/printer to collect the data. The load applied to the indenter was varied to take account of the following factors.

- (i) A large indent size will reduce proportionately the error resulting from inherent inaccuracies in measurement of that size.
- (ii) In order to give a reasonable result there must be no overlap of deformation caused by the indenter into the adjacent phase, across a grain boundary, or with a region deformed by a previous indent (Sargent, 1979a). This places an upper limit on what constitutes a reasonable size of indent, and hence on the load.

In consequence, an applied load of 0.981N was used for the ferritic regions of the microstructure, and 0.2452N for the (somewhat smaller) bainitic regions.

Subtle variations in microhardness with applied load are well documented, even for polycrystalline metal specimens (the so called indentation size effect). In general, the hardness is found to be increased for the smallest applied loads, a phenomenon which can be attributed in part to surface effects, *e.g.*, work hardened surfaces during specimen preparation, oxide and other surface films *etc.*, which are more pronounced for smaller indent sizes; in part to the fact that the dislocation loops associated with smaller indents are more sharply curved and require a correspondingly higher stress to propagate (Buckle, 1973; Sargent, 1979b). As a result the readings obtained for ferritic and bainitic regions are not mutually compatible, and identical loadings for all measurements on the same microstructural feature were used so that a quantization of variation of hardness with distance for a given microstructural feature could be obtained.

3.4.2 Results

The results are illustrated schematically on figure 3.5 for both longitudinal and transverse sections expressed in terms of the distance from the header bore. Between 40 and 60 readings were taken for each point on the figure, and the

point itself represents the mean of those readings, with the scatter bars on figure 3.5 representing standard deviations in those sets of figures.

A definite trend is shown clearly by figure 3.5: the microhardness of the bainitic regions is noticeably higher towards the inside surface of the pipe (the region where banding was observed), whereas the ferritic regions show an increased microhardness towards the outside surface (where the microstructure appeared more random). The standard errors calculated for each set of data indicate that it is reasonable to conclude that sufficient readings have been taken to verify this as a real microstructural effect and not a statistical aberration.

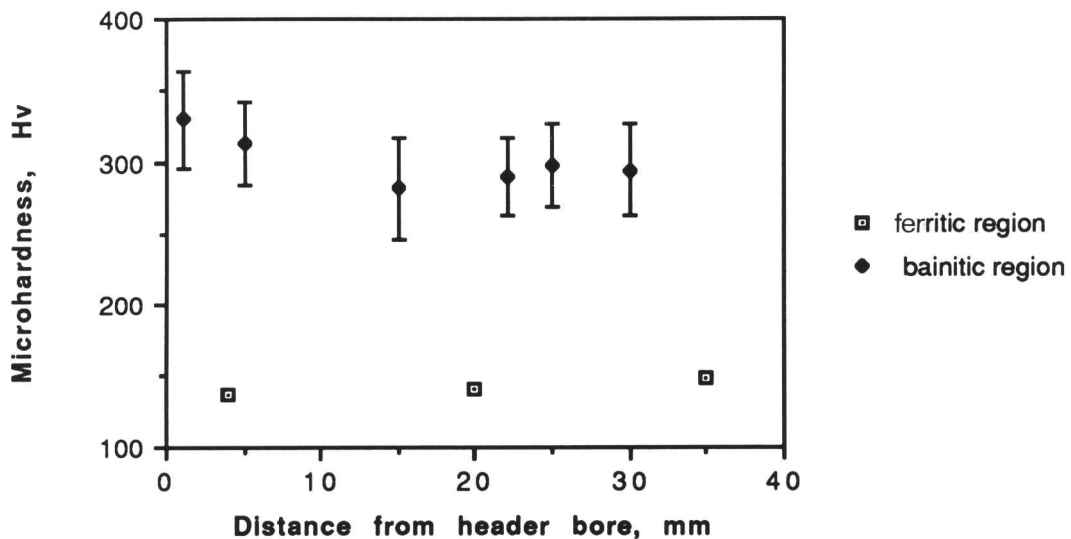


Figure 3.5: Microhardness measurements for the unexposed steam header material

3.4.3 Discussion

A lower microhardness in the ferrite could be attributable to a slower cooling rate during the initial transformation, hence a softer material, in some parts of the specimen. This would be expected to be accompanied by a larger ferrite grain size in these regions, and no such variation was observed. In a material where the ferrite grain size varies so much at adjacent points in the material, it would be very difficult to detect small systematic variations between different areas of the microstructure, so the absence of a detected variation does not definitively prove its absence; however, it is unlikely that such a small difference could be associated with any large effect.

An alternative explanation for the ferritic region could be provided by differences in distribution of carbides within the ferrite: relatively small changes in the structure and distribution of intragranular carbides, which could arise as a result of long-range chemical inhomogeneity in the original cast, would be expected to have a measurable effect on local hardness. However, metallography showed the intragranular carbide precipitates to be of a relatively uniform distribution.

The bainitic region has been shown (Section 3.3) to occupy a smaller volume fraction towards the bore of this piece of steam header than it does towards the outside surface. This would imply that the bainite contained a higher proportion of bainitic Fe_3C , more closely spaced; a microstructure which would be expected to produce a harder bainitic region, and is strongly indicative of a local variation in cooling rate between the two regions. A consideration of the likely transformation processes given the heat treatments to which the steam header had been subjected (appendix) implies that the material will be partially transformed to allotriomorphic ferrite, with bainite forming subsequently during cooling. It is possible to explain the fact that greater evidence of variations in temperature is seen in the bainite on this basis: if there was a variation in temperature during the air cool, a possibility for a component of significant thickness, then the effect on the bainitic region would be pronounced.

Studies of low-alloy ferritic steels in real systems are complicated by the possibility of both thermal variations during transformation and chemical heterogeneity. In the material examined here, the observed microstructural banding effect may well result from segregation effects within the original cast material which promoted aligned nucleation during the subsequent heat treatments, and it has been shown that local thermal and compositional variations in this material can make an appreciable difference to microstructural appearance and physical properties. Both these factors may potentially have contributed to the observed microstructure.

3.5 Energy Dispersive X-ray Analysis

3.5.1 Procedure

Microanalysis of the unexposed steam header material was carried out on a Cambridge Instruments ISI100 scanning electron microscope, which was fitted with a LINK energy dispersive X-ray analysis system. The resulting data were analysed using the LINK microanalysis programme (which includes corrections for fluorescence, atomic number, and absorption effects). A transverse section was taken and mounted in bakelite, which contained particles of graphite so that it would be electrically conducting; polished to $0.25\mu\text{m}$ diamond paste as for optical metallography; and given a very light etch in 2% nital (it was necessary to use an etchant in order to distinguish between ferrite and bainite, but to the minimum level so as to affect chemical composition as little as possible).

3.5.2 Theoretical basis of EDX technique

The EDX system collects and analyses the X-ray emission spectrum produced in the material by de-excitations of near-surface electrons which had been stimulated into an excited state by the scanning electron beam. The overall X-ray emission spectrum for the material is analysed (*e.g.*, figure 3.6), and the proportions of elements present calculated by quantification of the characteristic X-ray peaks for each element present.

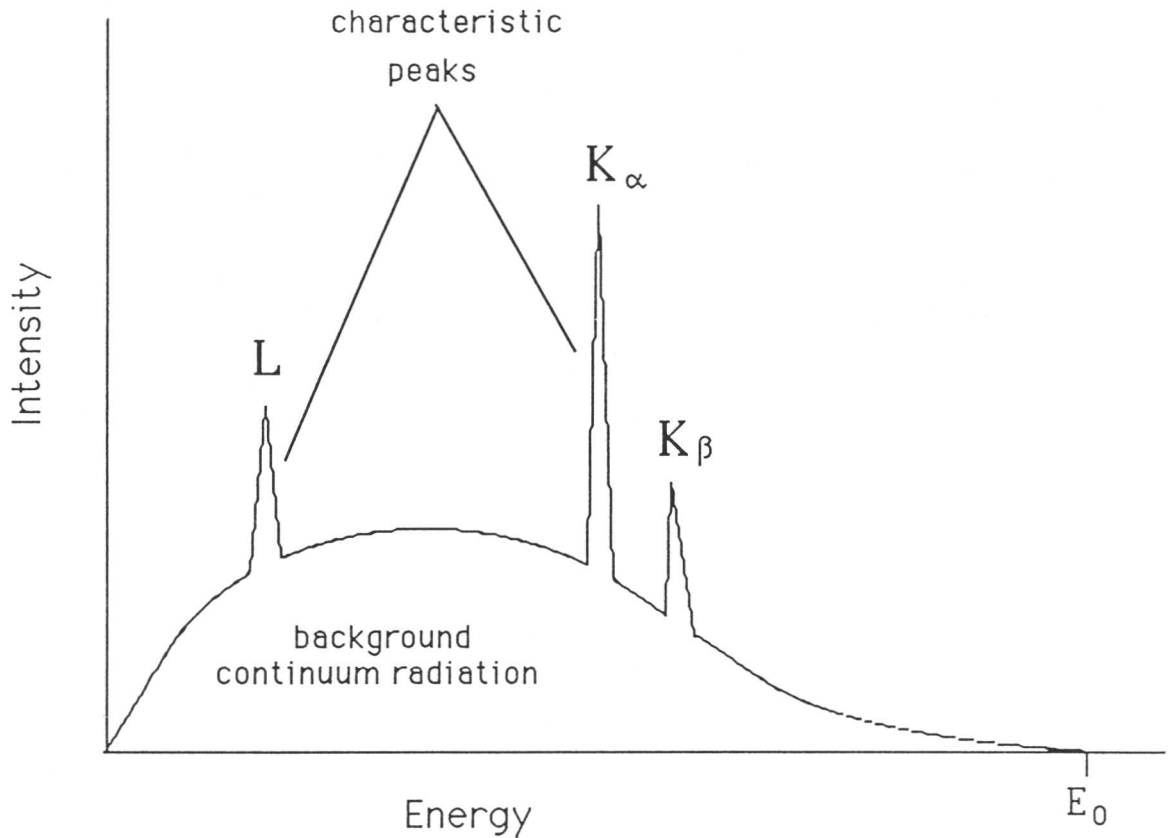


Figure 3.6: Typical X-ray emission spectrum

Note that EDX is not a surface sampling technique as it analyses emissions from a 'pear-shaped' envelope of material (figure 3.7). As a consequence, results must be treated with caution, as it is possible inadvertently to sample data from two different phases if the second phase lies just below the surface. Also, low-atomic-number emissions are absorbed by the system (see the typical spectrum), hence EDX is not a viable technique for detecting carbon, nitrogen, oxygen or hydrogen. (Russ, 1984)

3.5.3 Results

The results are presented in figure 3.8 for both the region near the bore and the region near the outside surface of the material. The spatial resolution can be considered to be approximately $10\mu\text{m}$. Mean values for each set of compositional readings for a particular point in the material were calculated, and are also

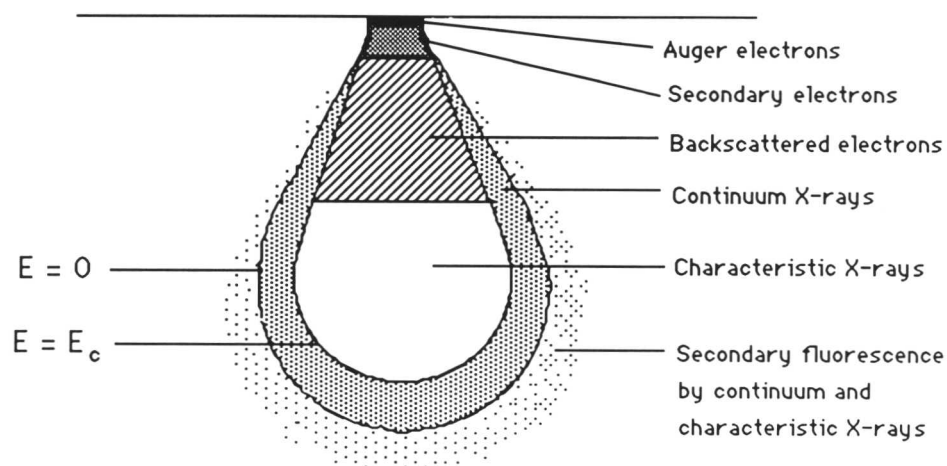


Figure 3.7: Volume sampled by EDX technique

included on figure 3.8 as horizontal lines, with the overall mean alloy composition marked on the y-axis. Standard errors in those means (calculated from the standard deviation) were all in the region ± 0.10 to ± 0.18 wt%.

It had been hoped that differences in composition between the banded and unbanded regions, which might suggest an explanation for the banding effect, would be exposed by this work. However, whilst the results are indicative of some variations in proportion of some alloying elements between ferrite and bainite, it seems impossible to draw any conclusions about small levels of local heterogeneity: the resolution of the technique is not adequate to respond to small composition changes between areas, given the large variations in composition which are apparently observed for different points of the same phase in the same area (probably due to the problems associated with the sampling envelope size mentioned above), and the values of standard error in the calculated means.

AS RECEIVED MATERIAL

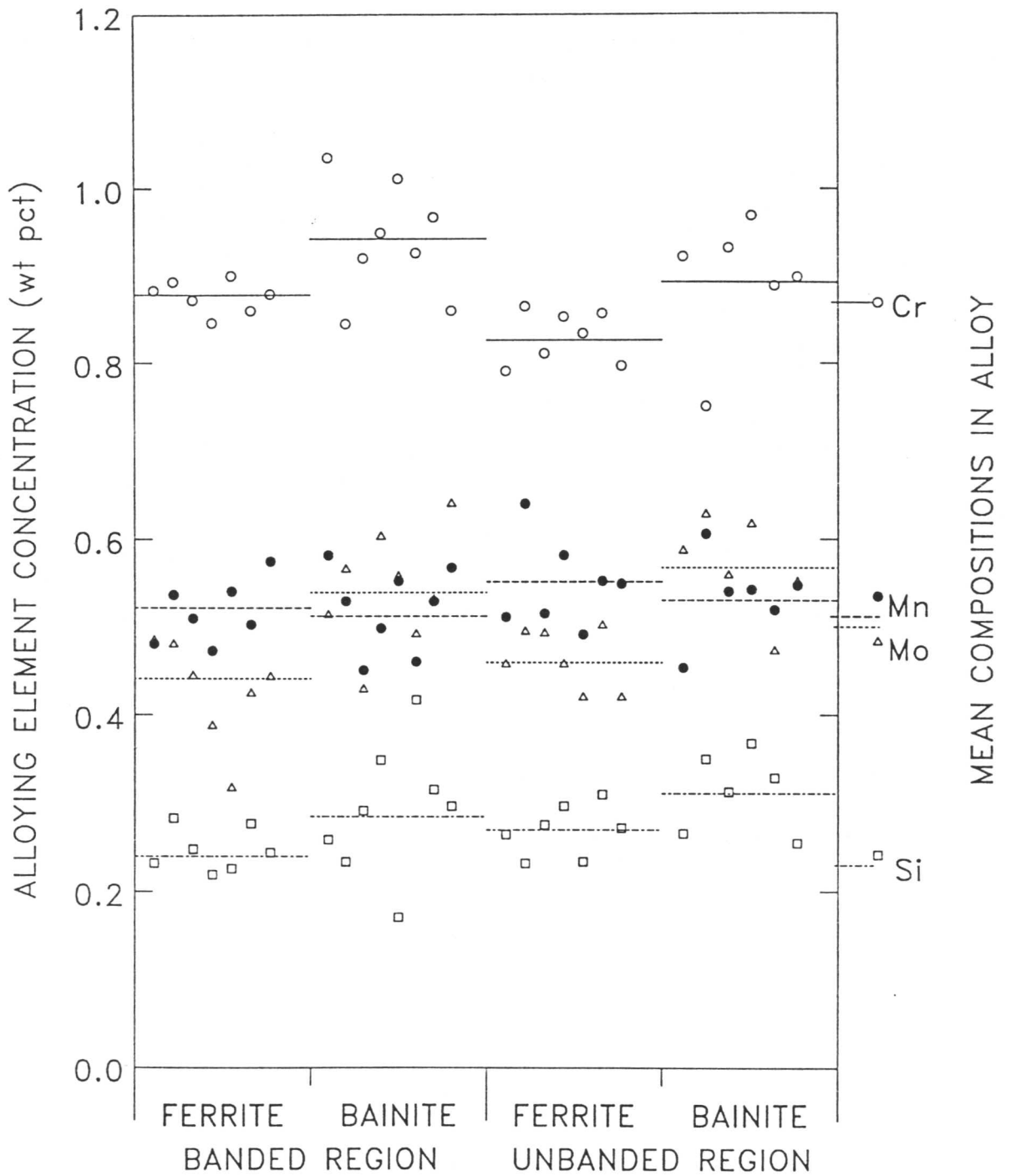


Figure 3.8: EDX compositional data for as-received steam header material

Even so, it is notable that the proportion of some alloying elements (*e.g.*, Cr and Mo) is consistently greater in the bainitic region, although by an amount which is within the error bounds. The regularity of this small variation suggests real difference is being represented, even if resolution is inadequate for the difference to be fully quantified. The EDX data is consistent with the hypothesis that some redistribution of substitutional alloying elements has taken place during ferrite formation at the point of fabrication, from ferrite to retained austenite. Such a redistribution would enrich the retained austenite, and thus the bainite which subsequently formed from the retained austenite would be similarly enriched. The silicon composition is relatively constant; in any case, if a partitioning effect were shown for this element, it would be in the other direction, from austenite to ferrite.

Moreover, the range of readings obtained is much greater for the bainitic than for the ferritic regions, and it is suggested that the larger chromium, manganese and molybdenum composition results were obtained where the volume sampled was mostly bainitic, and that results from apparently bainitic regions which are closer to those obtained from the ferrite arise because the sampled volume included an amount of allotriomorphic ferrite (perhaps just below a carbide region on the surface). This sampling volume problem would tend to mask any small differences which were present.

In conclusion, the EDX technique on the SEM is satisfactory for illustrating general compositional trends in this alloy, but the sampling volume is too large for quantitative data to be obtained on the small scale necessary to analyse compositional variations in individual carbide structures.

3.6 Summary

The microstructure of the pre-service steam header is a mixture of allotriomorphic ferrite and partially-annealed bainite, the bainite making up around 25% by volume. Observations provide evidence of inhomogeneity on both a microscopic and macroscopic scale in the as-received sample, with a suggestion of both chemical inhomogeneities in the original cast and localized temperature

variations during the heat treatments used in fabrication of the steam header section.

These observations are in agreement with much previously published work on the microstructure of low-alloy ferritic steels and the problem of inhomogeneity in steam header material. It is essential that this inhomogeneity is considered, and an attempt made to quantify its rôle in microstructural development during ageing, if an improved remanent creep life prediction model which is applicable to real systems is to be developed.

Chapter 4

MODELLING THE AUSTENITE–FERRITE TRANSFORMATION

4.1 Introduction

Phase diagrams and TTT curves are of considerable value in predicting and understanding phase changes. For this reason, calculations using a model to predict the phase boundaries and transformation start times in low-alloy steels have been performed for the compositions corresponding to those of the supplied power plant material. The procedure was repeated for an Fe–4.08Cr–0.3C (wt. %) alloy, which was used in subsequent experimental work as an alloy to study the model proposed by Bhadeshia (1989) for the ageing of bainitic cementite.

Further calculations for the power plant steel were performed to provide an illustration of the effect of variations in composition (which could arise due to segregation effects) on the TTT curves, and hence the transformation process and products. The existence of some macrosegregation in practice was shown by comparing measured compositions of two specimens taken from a real, service exposed component, both of which came from the same initial cast, but had been found to have slightly different compositions thus illustrating compositional inhomogeneity in a real system. These samples were also of the 1Cr– $\frac{1}{2}$ Mo type steel. (full details of the composition and fabrication of all these steels may be found in Appendix 1.)

The calculated data were compared with an experimentally-determined TTT curve produced by dilatometric work carried out on homogenized and reaustenitized specimens of the power plant material. The microstructures thus generated were prepared for optical examination, and a comparison made between the appearance of the regenerated microstructures and the observations made in the previous chapter of material in the as-received condition.

4.2 Theoretical Calculation of TTT Diagrams

4.2.1 The model

A computer program has been developed to generate TTT diagrams for low-alloy steels containing carbon, silicon, manganese, nickel, molybdenum, chromium and vanadium (Bhadeshia, 1982). It is based on a model to calculate reaction start times for the different austenite-ferrite reaction products at varying transformation temperatures and compositions.

'C'-curves can then be predicted for both reconstructive and displacive reactions as a function of time and temperature with a reasonable degree of accuracy; limitations are imposed because only certain alloying elements are considered, and because the approach is applicable only to low levels of substitutional alloying (typically less than about 7 wt%). The model generates reaction incubation times which are not especially sensitive to grain size, so the results are consistent for varying grain size. Provided the limitations of the low-solute approximations in the model are borne in mind, the calculations made by the program should be able to provide a reasonable quantitative guide to the effect of alloy heterogeneity on transformation rates and products.

The method was essentially developed by fitting experimental values to the general equation of incubation time proposed by Russell (1969), that is

$$\tau_s \propto \frac{T}{(\Delta F_m^v)^p D} \quad (4.1)$$

where τ_s is the incubation time taken to establish a steady nucleation rate,

T is the absolute temperature,

D is the appropriate diffusion coefficient,

ΔF_m^v is the maximum volume free energy for nucleation (and is a function of alloying element concentrations and transformation temperature),

and p is an exponential factor which depends on the nature of the nucleus (Russell showed theoretically that $p = 2$ for a coherent nucleus, $p = 3$ for an incoherent one).

Thus, two C-curves were generated, representing reconstructive and displacive transformation incubation times as a function of time and temperature in the materials under investigation. The method allows the effect of varying alloying element concentrations on τ to be studied in some detail. The TTT curves that were generated from calculations applying this model to the 1Cr- $\frac{1}{2}$ Mo type power plant steel and the Fe-4.08Cr-0.3C wt % model alloy are shown by the continuous lines on figure 4.1 and figure 4.2 respectively.

4.2.2 Long-range segregation of alloying elements

The model may also be used to calculate partition coefficients between liquid and solid, and from these the compositions corresponding to maximum solute depletion during solidification for the four power plant alloy compositions (the unexposed header material, service exposed plugs U3B1 and U4A1, and the base cast composition of the service exposed material). An estimate of the maximum solute enrichment can be obtained by reversing the calculation. TTT curves calculated for these new compositions will provide an illustration of the effect which chemical segregation could have on the transformation behaviour of the material. The calculated maximum solute depleted and maximum solute enriched compositions are presented in table 4.1, and TTT curves corresponding to those compositions for the steam header section are plotted from the computer model and superimposed on that for the original composition (the broken lines on figure 4.1) for comparison purposes.

An examination of table 4.1 also illustrates levels of compositional inhomogeneity which may be observed in practice, as shown by the differences between the measured compositions of the two service exposed plugs, U3B1 and U4A1, which were taken from the same cast. It can be suggested that the very large size of these components leads to a cooling rate during casting which is sufficiently slow to allow some redistribution of alloying elements, and produce inhomogeneity of composition.

Specimen	Compositions (wt.%)								Transformation starts, °C	
	C	Si	Mn	Ni	Mo	Cr	V	B _s	M _s	
<i>steam pipe section</i>	SD	0.12	0.16	0.38	0.00	0.25	0.72	0.00	601	483
	OC	0.12	0.23	0.51	0.00	0.50	0.87	0.00	594	474
	SE	0.12	0.33	0.68	0.00	1.00	1.05	0.00	580	458
<i>U3B1 plug</i>	SD	0.11	0.14	0.32	0.06	0.27	0.74	0.00	604	488
	OC	0.11	0.19	0.43	0.12	0.54	0.89	0.00	594	477
	SE	0.11	0.27	0.52	0.27	1.10	1.08	0.00	578	459
<i>U4A1 plug</i>	SD	0.13	0.16	0.39	0.06	0.26	0.84	0.00	595	475
	OC	0.13	0.22	0.52	0.13	0.53	1.02	0.00	581	461
	SE	0.13	0.31	0.69	0.29	1.06	1.24	0.00	566	442
<i>base header cast</i>	SD	0.13	0.18	0.41	0.07	0.27	0.84	0.00	594	474
	OC	0.13	0.25	0.55	0.14	0.54	1.01	0.00	580	460
	SE	0.13	0.35	0.73	0.31	1.10	1.22	0.00	559	438

OC denotes the base composition of each material, and SD and SE denote results for solute depleted and enriched compositions (for maximum segregation)

Table 4.1: Theoretical analysis of effects of segregation

4.2.3 Discussion

It is hoped that the predicted TTT diagrams will be of value when used together with heat treatment experiments to monitor the transformation as it proceeds, and microanalysis in order to determine the levels of segregation of alloying elements and the effect of this on the resulting development of microstructure.

Although segregation effects on the TTT curves for the power plant material are apparently small the effect on microstructure may be exaggerated. Depending on the cooling processes used, the nature of the transformation products (both which form first and their relative proportions) could change. Segregation is known to be considerable in these materials in practice, both on a microscopic level, and macroscopically with variations in different parts

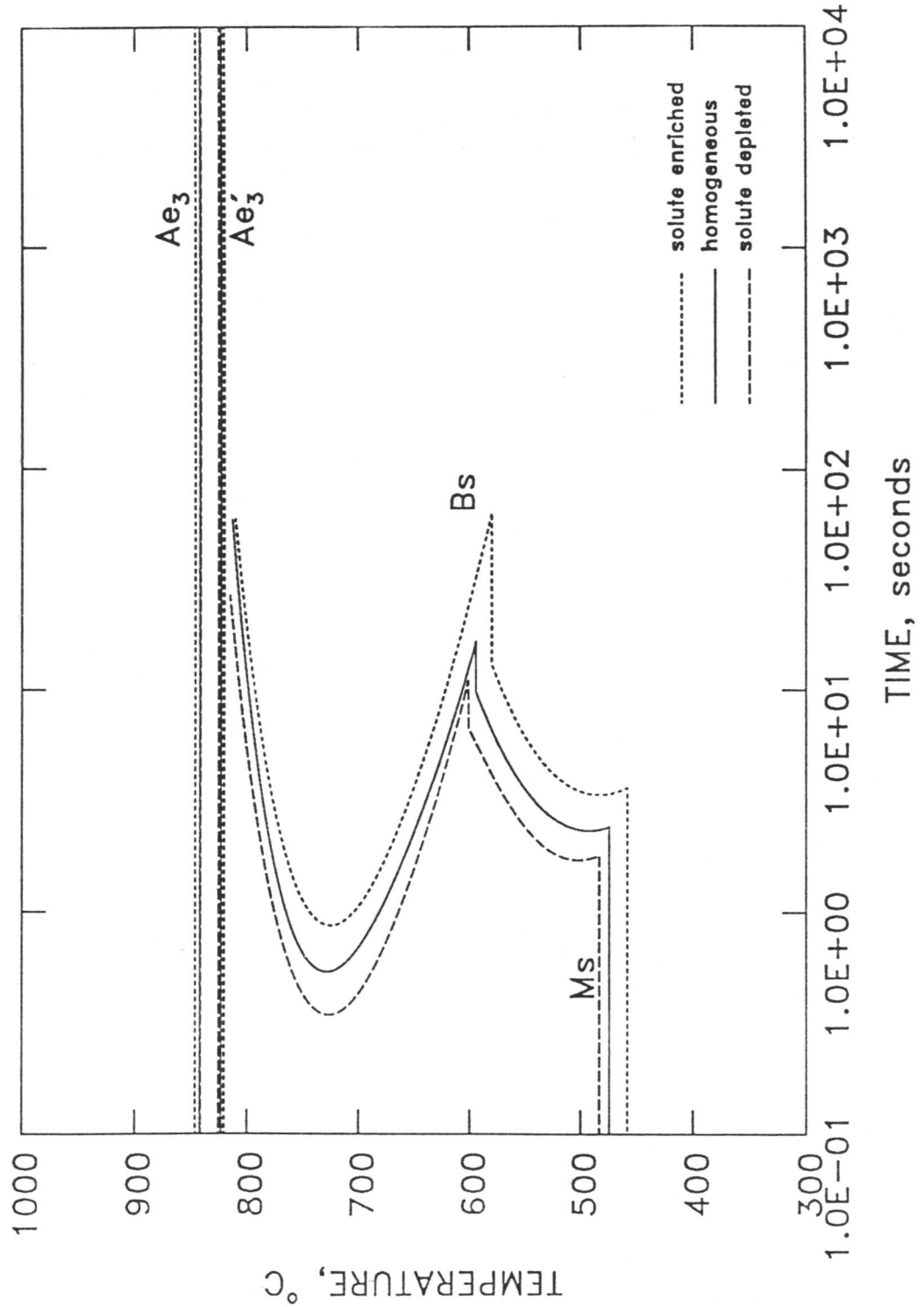


Figure 4.1: Calculated isothermal TTT diagram for the unexposed steam header material

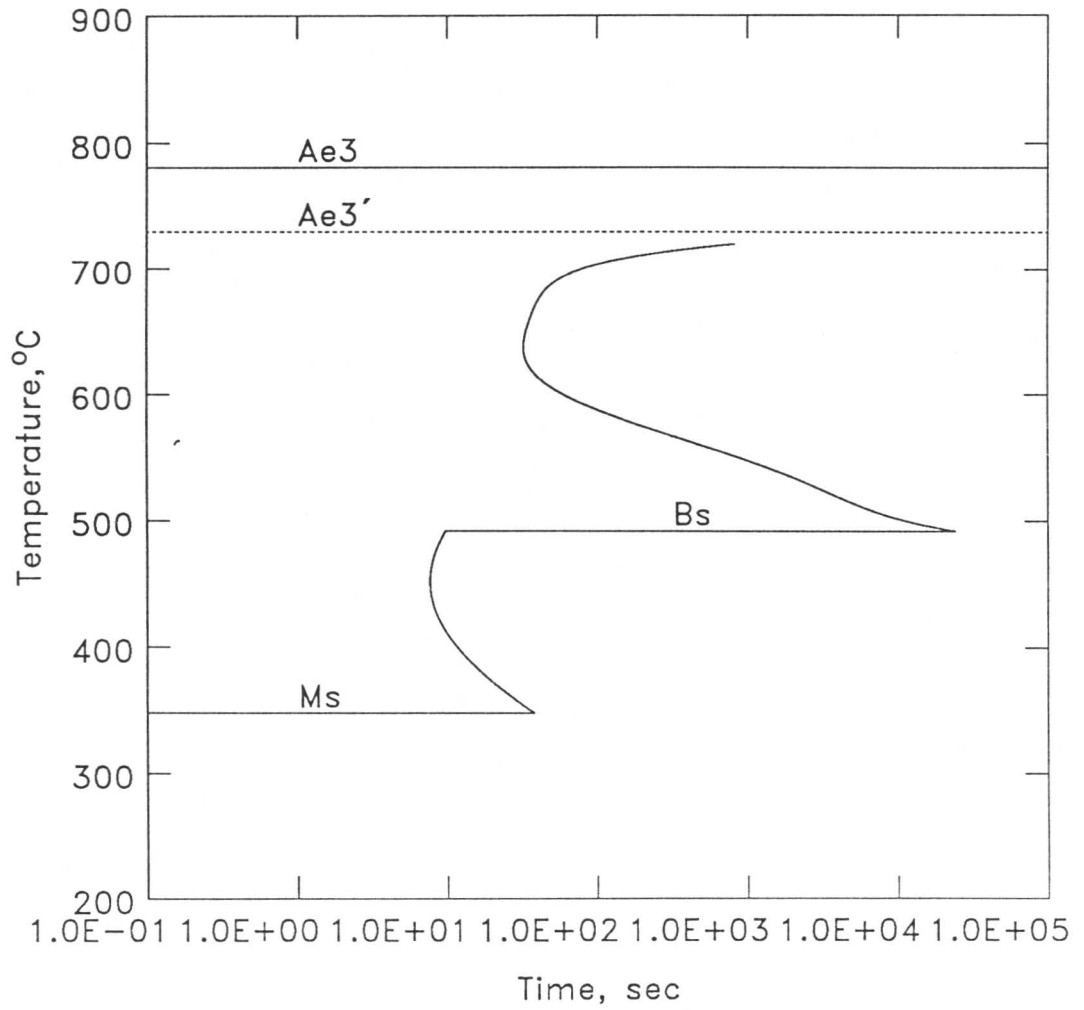


Figure 4.2: Calculated isothermal TTT diagram for the Fe-4.08Cr-0.3C (wt %) model alloy

of a cast ingot (for example, see the differences in composition between U3B1 and U4A1 plugs – both from the same cast – in the appendix). As a result, obtaining an idea (even if only approximate) of the effect of segregation on the transformation in low-alloy ferritic steels of these compositions is of considerable value.

4.3 Calculation of Phase Diagrams

4.3.1 *The model*

A computer program has been developed based on thermodynamic models proposed by Bhadeshia (1981a). This provides a procedure to enable the T_0 , T'_0 and Ae'_3 curves to be calculated for the alloy compositions under consideration.

T_0 is defined as the temperature at which α and γ of the same composition have the same free energy (Zener, 1946). It lies between the Ae_1 and Ae_3 temperatures which define the limits of the $\alpha + \gamma$ two phase field. Above T_0 ferrite growth can only occur accompanied by a change in composition. Bainite has been observed to form via a displacive mechanism with associated invariant plane strain shape change; the curve for T'_0 is the T_0 curve modified to take account of the 400 Jmol^{-1} strain energy accompanying the IPS. The displacive bainite transformation mechanism implies that no composition change occurs during transformation, which is therefore impossible above this temperature.

Ae'_3 is the equivalent to Ae_3 (the curve representing the boundary between the $\alpha + \gamma/\gamma$ phase fields), but modified to apply to the para-equilibrium situation. This differs from the Ae_3 temperature because for paraE no redistribution of substitutional alloying elements occurs during transformation, and the substitutional atom to iron atom ratio is constant throughout the material.

4.3.2 *Calculated results*

The T_0 , T'_0 and Ae'_3 curves were calculated for alloying element concentrations corresponding to that in the unexposed steam header material and in the Fe-4.08Cr-0.3C (wt %) model alloy. These are represented graphically in figure 4.3 and 4.4, as a function of carbon content.

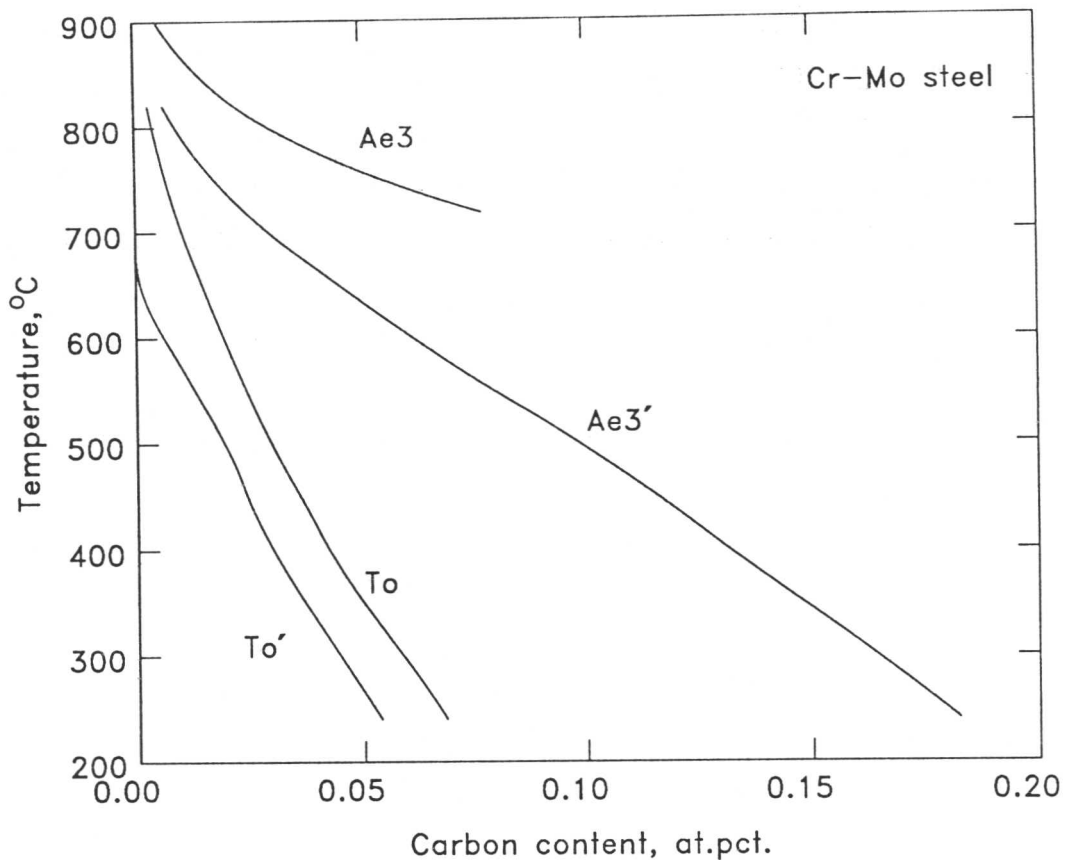


Figure 4.3: Calculated T_0 , T'_0 and Ae'_3 curves for the $1\text{Cr}-\frac{1}{2}\text{Mo}$ as-received power plant material

4.4 Heat Treatments on Steam Header Section

4.4.1 Aims of experimental work

It was the intention of this work to try to recreate the microstructure of a pre-service steam header material (based as closely as possible on the observations discussed earlier which were made of specimens from the actual pre-service material) by repeating the heat treatments used in fabrication on regenerated material. The procedure was designed to enable all the austenite-ferrite transformation processes in this alloy to be studied in some detail, and thus give a sound basis on which to determine the heat treatments necessary to reproduce the starting microstructure and conduct subsequent microstructural assessment when the material was aged to model service conditions.

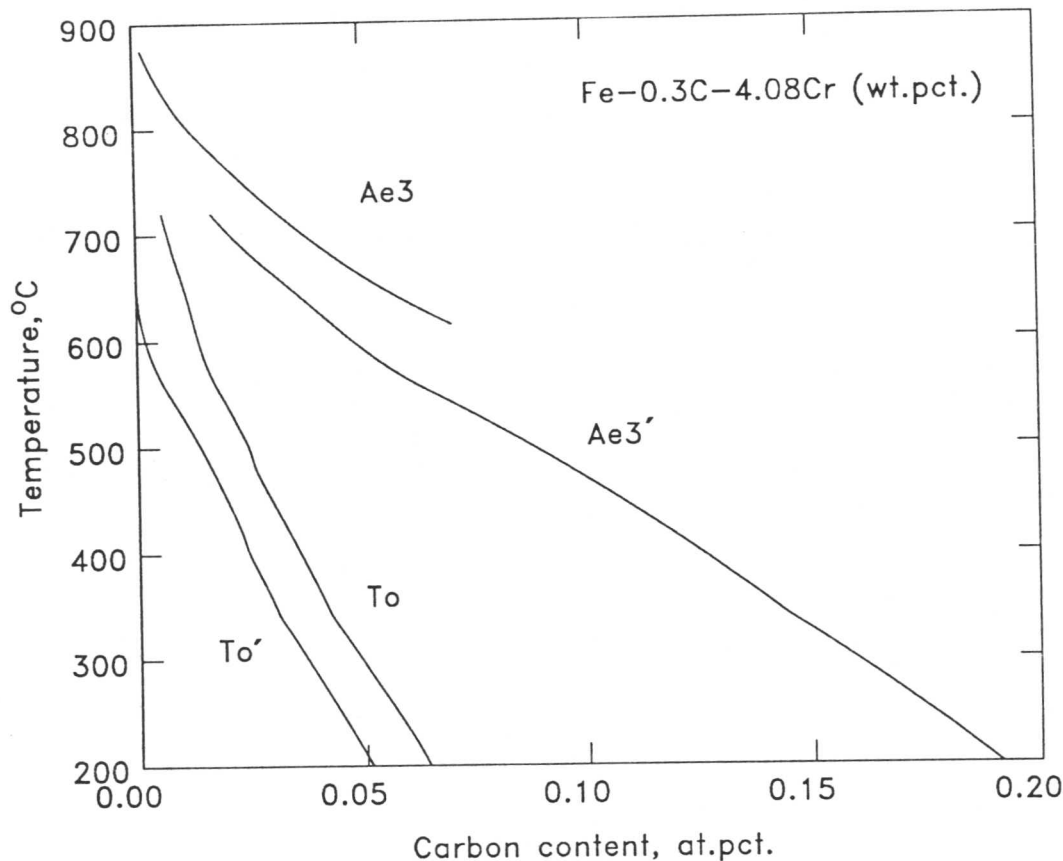


Figure 4.4: Calculated T_0 , T'_0 and Ae'_3 curves for the Fe-4.08Cr-0.3C (wt %) alloy

To this end a large number of 3mm diameter rods were machined from the steam header section. These rods were sealed in a quartz tube, which had been evacuated and had a partial pressure of argon (160 mm Hg) inserted to prevent the loss of carbon from the surface due to vaporization; homogenized by heating in a tube furnace at a temperature of 1250°C for 3 days; and then air cooled, still inside the sealed tubes to prevent environmental attack on the surface during cooling.

It was the intention of the procedure to model thick-section material using a 3 mm diameter rod, so it was essential that any surface nucleation effects should be kept to a minimum if the results were to be at all representative. (In a steam header the low surface to volume ratio renders surface effects negligible, whereas for small rods they could be significant.) As a result all specimens were nickel

plated before heat treatment. The treatment involved two processes: an initial striking and subsequent plating. The striking solution consisted of 250g NiSO₄ and 27ml of conc. H₂SO₄ made up to 1 litre by addition of the appropriate quantity of distilled water. Striking was carried out for 3 minutes at 50°C and a current density of 775mAcm⁻². The plating solution was 140g NiSO₄, 140g Na₂SO₄, 15g ammonium chloride and 20g boric acid made up to 1 litre in distilled water. Plating was carried out for 15 minutes at 50°C and a current density of 40mAcm⁻².

4.4.2 High-speed dilatometer

This machine was used to carry out the austenitizations and transformations back to ferrite on the homogenized steam header material. It operates by measuring and recording the length change which takes place in the specimen under test as the temperature is varied. This allows the transformation to be monitored, by recording the volume expansion that takes place as austenite is transformed to ferrite.

The set up of the dilatometer is illustrated schematically in figure 4.5. The specimen is fixed between two quartz tubes, one of which is static, and the other free to move as the specimen expands or contracts; the latter tube is attached to a linear transducer, which enables length change to be recorded. Heating is achieved by use of an RF induction coil which enables quite rapid heating rates to be obtained. The specimen is enclosed in another quartz tube to prevent contact with the coil, and also to act as a safety barrier in the event of an equipment malfunction causing the specimen to melt. The surface temperature of the specimen is monitored by means of a Pt Pt-10wt%Rh thermocouple which is spot welded to the surface near the centre of the specimen length. The specimens are sufficiently small that it is reasonable to assume that the temperature is uniform throughout at the heating and cooling rates that the dilatometer produces. Helium is used to increase the cooling rate, by providing an inert quenching fluid should it be required; it may also be used to provide an inert atmosphere if a high vacuum is not desirable.

The procedure used to operate the dilatometer was as follows:

- (i) Before use the dilatometer transducer had been calibrated using a platinum specimen of accurately known thermal expansivity, so that data produced by the transducer for the steel specimens could be converted to accurate length change values.
- (ii) The specimen was set up as in figure 4.5.
- (iii) The transducer was 'tuned' by use of the attached micrometer (see figure 4.5) so that a suitable magnification for the chart recorder could be set, and temperature and length change pens on the chart recorder were zeroed.
- (iv) After pumping down to a good vacuum the specimen was raised to the austenitizing temperature and held there for a set austenitization period. Cooling was effected either by using a 'data-trak' program drum (for continuous cooling) or by quenching using the helium flux until the desired temperature was reached, and then holding at temperature (for isothermal transformation).

4.4.3 Heat treatments

Homogenized and nickel-plated specimens were given heat treatments over a range of temperatures and time scales. All of the specimens for isothermal transformation were first austenitized for 10 minutes at 1100°C, then quenched to the required isothermal temperature using the helium flux. Isothermal transformation temperatures were in the range 750°C to 450°C, allowing all transformation products from allotriomorphic ferrite to martensite to be produced, and transformation times were in the range 30 minutes to 2 hours. After completion of the desired transformation time, the material was allowed to cool by switching off the RF coil (note that for such small specimens this amounted to a fairly rapid quench). The dilatometer apparatus enabled readings for temperature and length (which could be converted to relative length change using the length at ambient temperature) to be taken at suitable time intervals. These data were collected directly onto computer disc for subsequent processing.

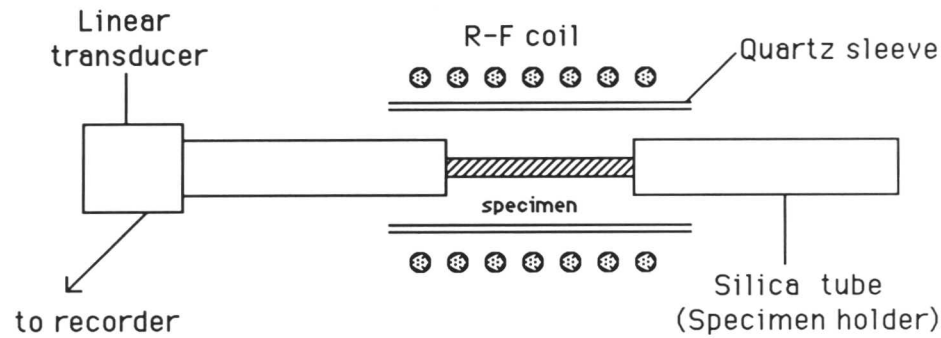
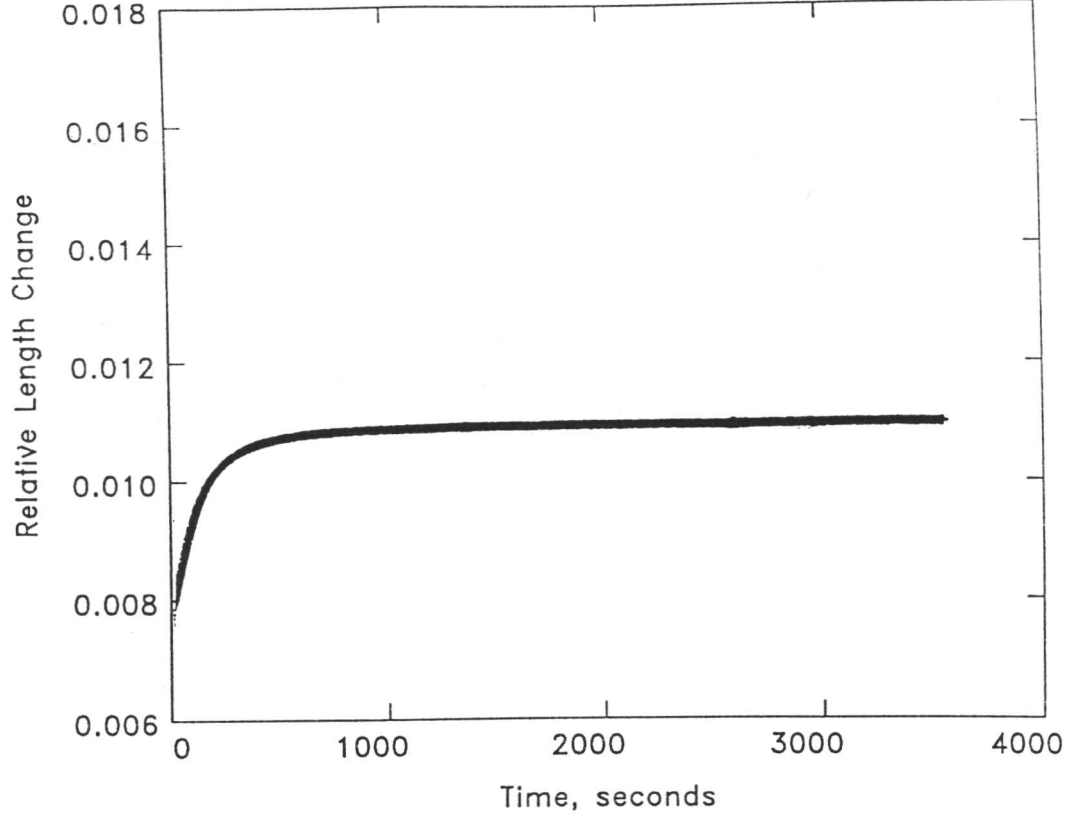


Figure 4.5: Dilatometer arrangement

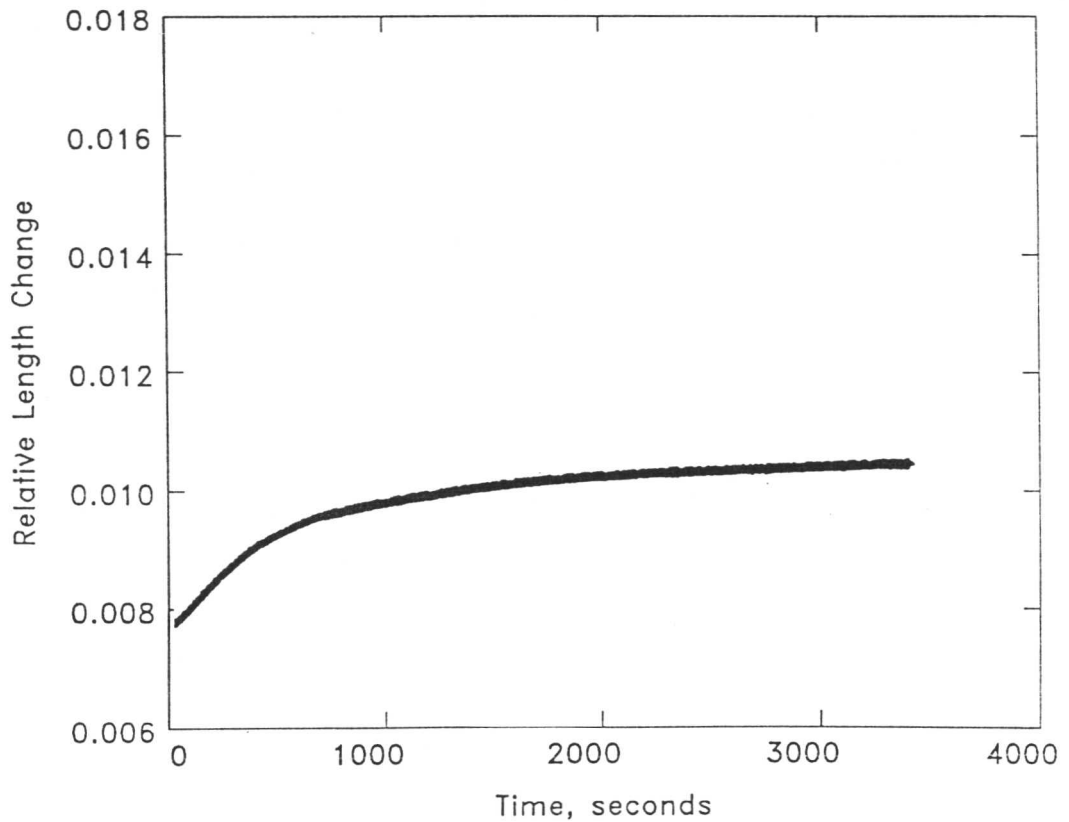
4.5 Results of Dilatometric Experiments

4.5.1 Processing of dilatometric data

Graphs illustrating the observed length change during the course of the transformation were obtained from the recorded data. The lower density of the ferritic structures compared with austenite manifests itself in a length extension as the transformation proceeds, and can be detected by the transducer. Typical examples of such plots are given in figure 4.6, each data point having been collected at one second intervals in all four cases. The data were processed to determine the transformation start time and the volume fraction transformed at a given temperature; the latter was determined both by direct measurement using a point counting technique, and by calculation from dilatometric length change data. These calculations are discussed in detail below, and the processed dilatometric data are presented in table 4.2. The rapid progress of the martensitic transformation compared to transformations above M_s is clearly illustrated by figure 4.6(d).

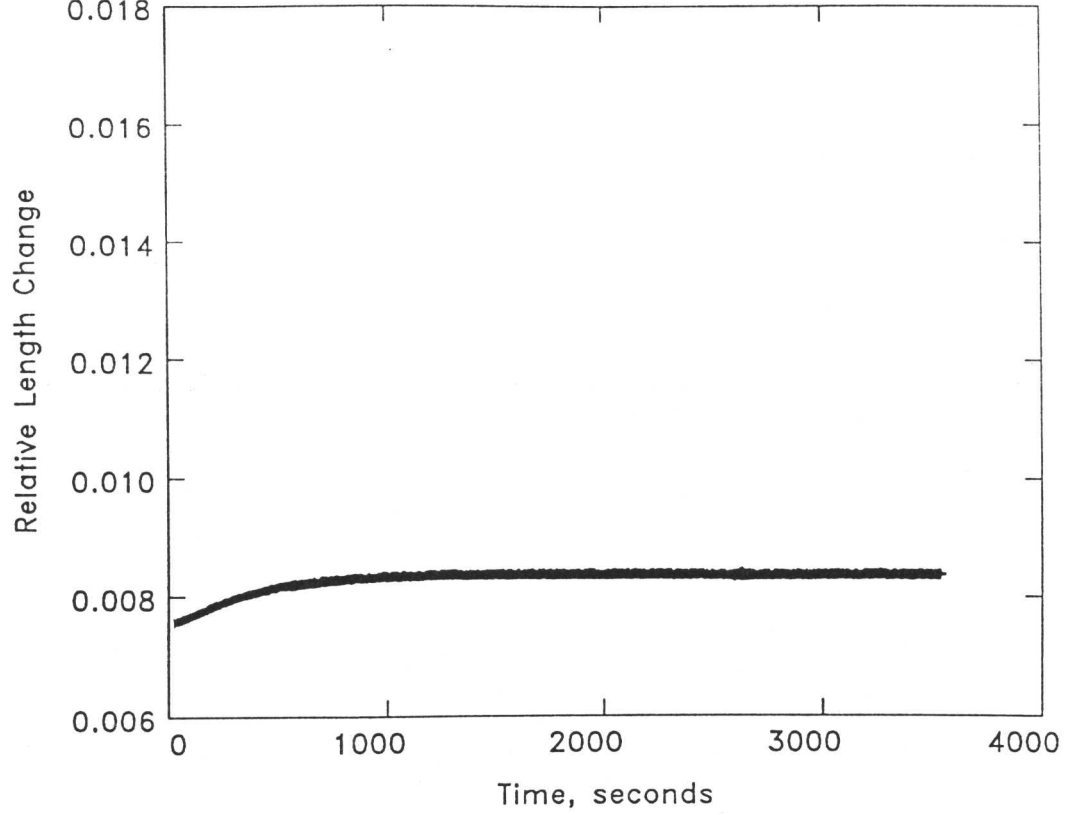


(a) 1 hour @ 735°C

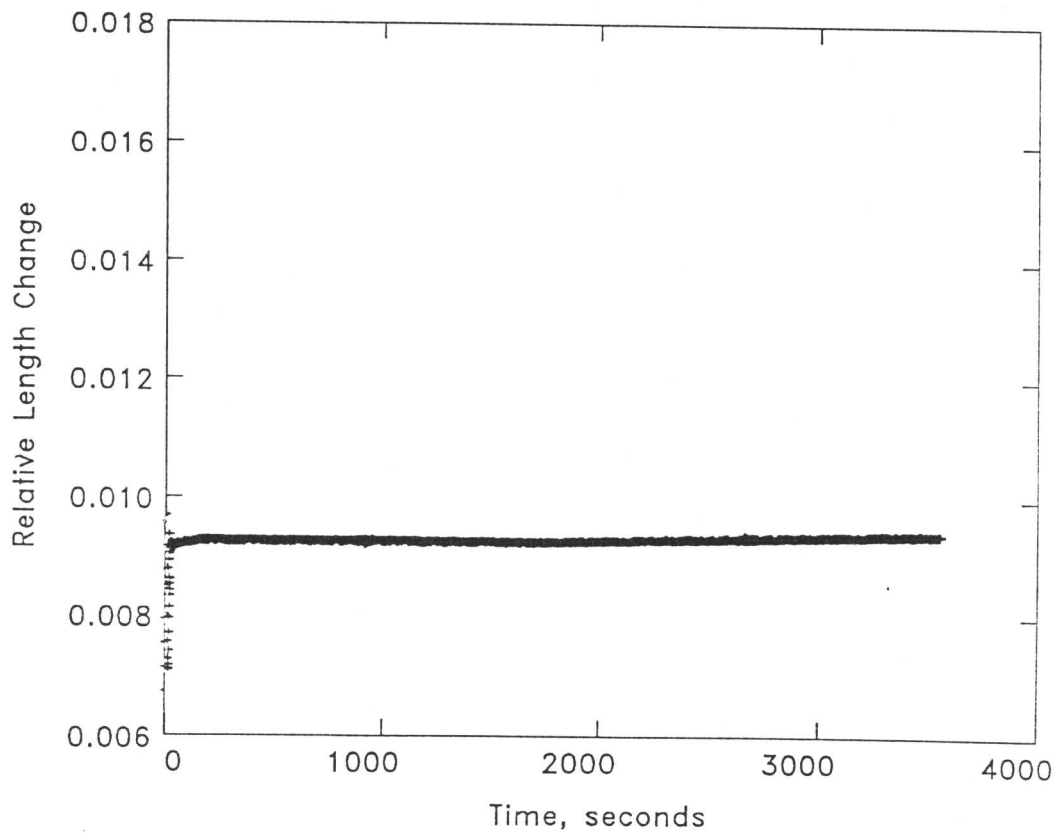


(b) 1 hour @ 647°C

Figure 4.6: Typical dilatometric relative length change vs time plots for isothermal heat treatments carried out on the 1Cr-1/2Mo power plant steel



(c) 1 hour @ 547°C



(d) 1 hour @ 453°C

Figure 4.6: Typical dilatometric relative length change vs time plots for isothermal heat treatments carried out on the 1Cr- $\frac{1}{2}$ Mo power plant steel

4.5.2 Transformation incubation times

It was possible to extract the data points applying to the early stages of each experimental run and plot graphs of length *versus* time for these limited periods. From such plots the time taken for the reaction to commence (the point at which the length began to increase at constant temperature) could be determined with reasonable accuracy. A temperature vs. time plot of the same period was also required in order to ascertain the time which elapsed during the experimental run before the desired isothermal temperature was reached; this must be subtracted from the total time to give a correct incubation time for that particular transformation temperature. The procedure is illustrated in figure 4.7. Note that the difficulty in determining exactly the point at which a length change at constant temperature (*i.e.*, a transformation from austenite to ferrite) first occurred can be considered to introduce an error of the order of several seconds to the tabulated incubation times. Those dilatometry runs in which no discernible period of time elapsed at the transformation temperature before a length change was observed (*i.e.*, the transformation start was, within the limits imposed by the technique, effectively instantaneous) are denoted on table 4.2 by ** in the incubation time column.

4.5.3 Determination of expansion coefficients

In order to translate relative length changes to volume fraction of transformed product it is necessary to determine the thermal expansion coefficients of both parent (austenite) and product (ferrite) phases, denoted by e_γ and e_α respectively. This was achieved by performing a continuous cooling dilatometry run for both ferritic and austenitic examples of the homogenized steam header material. The ferritic specimen was held for two hours at 800°C to try to ensure that it was fully spherodized.

The situation is complicated by the fact that the thermal expansion coefficient for ferrite in low-alloy steel materials are known to show an appreciable temperature dependence (Coleman & Rowley, 1973). Typical examples of this non-linearity in thermal expansion as observed in materials commonly used in

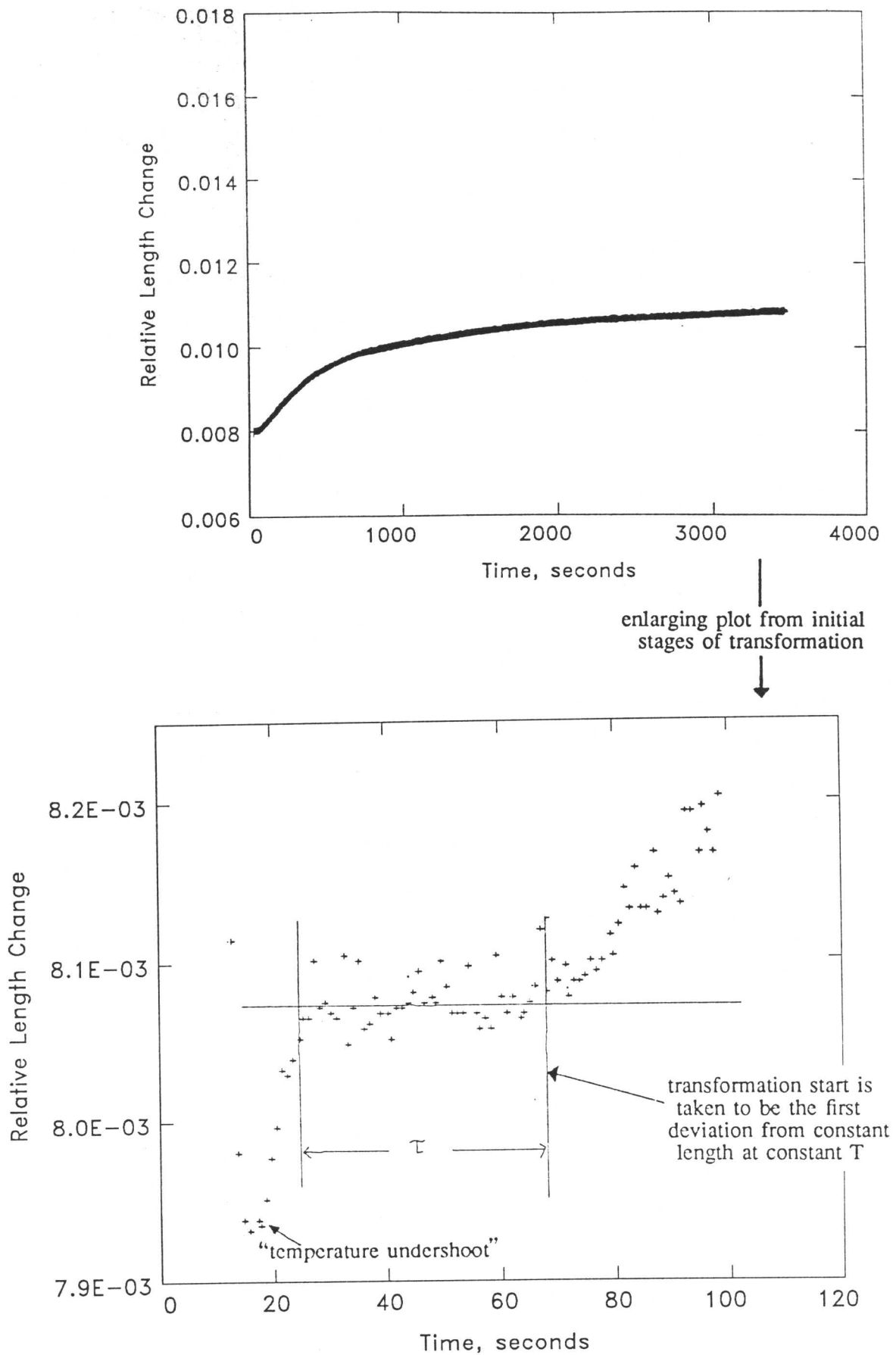


Figure 4.7: Determining transformation incubation times from dilatometric data

T_{iso}	t_{iso}	cooling time	τ	volume fraction of transformed region	
				measured	calculated
770°C	1 hr	15°C	85s	0.65	0.57
751°C	1 hr	15°C	30s	0.60	0.57
735°C	1 hr	12°C	10s	0.78	0.72
722°C	1 hr	11°C	4s	0.63	0.79
715°C	1 hr	10°C	**	0.80	0.85
703°C	1 hr	10°C	**	0.74	0.85
698°C	1 hr	20°C	3s	0.82	0.78
676°C	1 hr	10°C	3s	0.82	0.86
674°C	1 hr	12°C	13s	0.72	0.79
669°C	1 hr	20°C	5s	0.81	0.84
647°C	1 hr	12°C	30s	0.79	0.84
622°C	1 hr	8°C	16s	0.60	0.52
610°C	1 hr	8°C	12s	0.60	0.57
591°C	1 hr	12°C	22s	0.60	0.53
576°C	1 hr	15°C	70s	-	0.15
555°C	1 hr	6°C	20s	-	0.12
542°C	1 hr	10°C	36s	-	0.24
525°C	1 hr	8°C	12s	-	0.25
510°C	1 hr	12°C	7s	-	0.25
499°C	1 hr	15°C	15s	-	0.31
475°C	1 hr	5°C	**	all martensite	
453°C	1 hr	8°C	**	all martensite	
740°C	30 mins	12°C	3s	0.78	0.75
734°C	30 mins	15°C	9s	0.79	0.82
720°C	30 mins	15°C	**	0.82	0.79
703°C	30 mins	7°C	**	0.85	0.93
680°C	30 mins	12°C	2s	0.73	0.86
661°C	30 mins	10°C	25s	0.60	0.57
630°C	30 mins	12°C	18s	0.50	0.42
606°C	30 mins	10°C	80s	0.48	0.53
580°C	30 mins	12°C	44s	0.48	0.42
530°C	30 mins	15°C	12s	-	0.15
730°C	2 hrs	8°C	28s	0.88	0.92
693°C	2 hrs	10°C	**	0.90	0.93
640°C	2 hrs	7°C	15s	0.88	0.85
621°C	2 hrs	12°C	19s	0.72	0.88

Table 4.2: Dilatometric data produced for the 1Cr- $\frac{1}{2}$ Mo power plant steel during isothermal austenite-ferrite heat treatments

power plant construction are shown in table 4.3 and represented as a function of the temperature range on figure 4.8 (Darbyshire & Knight, 1977).

Temperature Interval °C	25 to 100	25 to 200	25 to 300	25 to 400	25 to 500	25 to 600	25 to 700
$\frac{1}{2}\text{Cr}\frac{1}{2}\text{Mo}\frac{1}{4}\text{V}$	12.02	12.55	13.20	13.80	14.36	14.90	15.31
$2\frac{1}{4}\text{Cr}1\text{Mo}$	11.75	12.21	12.77	13.30	13.81	14.31	14.73
$1\text{Cr}\frac{1}{2}\text{Mo}$	12.02	12.26	12.88	13.46	14.04	14.57	14.99
Mild Steel	12.22	12.78	13.39	13.94	14.49	15.05	15.47

Table 4.3: Mean coefficient of linear thermal expansion (in $\text{K}^{-1} \times 10^{-6}$) for some typical power plant steels (Darbyshire and Knight, 1977)

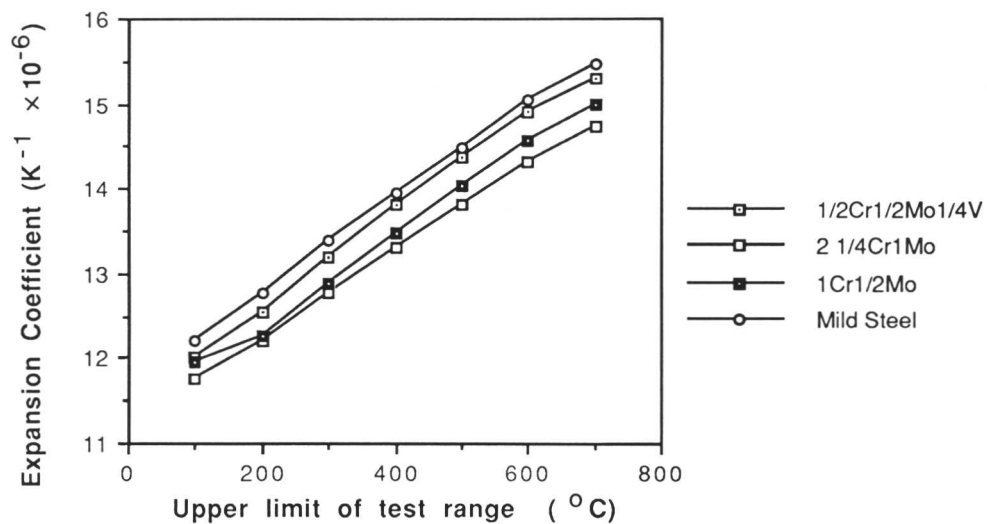


Figure 4.8: Variation as a function of T_{test} of the coefficient of linear thermal expansion (in $\text{K}^{-1} \times 10^{-6}$) measured over a range $25^\circ\text{C} - T_{\text{test}}$ for some typical power plant steels (Darbyshire and Knight, 1977)

The measured expansion coefficient for the steam header material will thus be expected to depend on the range of temperatures over which it is determined; hence, values appropriate to several temperature ranges have been obtained for the ferritic thermal expansion coefficients, as can be seen from table 4.4. These results are also presented graphically (figure 4.9) to illustrate the variation of thermal expansion coefficient with temperature in the steam header material used in this study. The initial length of the specimen is measured using a micrometer at ambient temperature, (T_{amb}); the specimen is then fully spherodized at around 800°C in all cases before being allowed to stabilize at the required test temperature, (T_{test}), at which point the length is determined from dilatometric data; then cooled slowly to T_{amb} in order to allow the linear thermal expansion coefficient specific to the range $T_{amb}-T_{test}$ to be determined.

Temperature Interval °C	25 to 100	25 to 200	25 to 300	25 to 400	25 to 500	25 to 600	25 to 700
Value of e_{α}	11.90	13.07	13.27	14.11	14.73	14.99	15.60
Value of e_{γ}	33.1						

Table 4.4: Mean coefficient of linear thermal expansion (in $K^{-1} \times 10^{-6}$) as determined from dilatometric experiments carried out using the 1Cr- $\frac{1}{2}$ Mo type power plant steel

4.5.4 Measuring volume fraction of transformed material

Two approaches were used to obtain these results. Firstly, optical specimens were prepared, polished down to 0.25 μm diamond paste, and etched in a solution of 2% nital. The region which had remained untransformed at the end of the dilatometer run was clearly visible as a martensitic region, the product of retained austenite during the period of rapid specimen cooling after the furnace was switched off at the end of the run. This observable difference allows a systematic point-counting method to be used to determine the relative

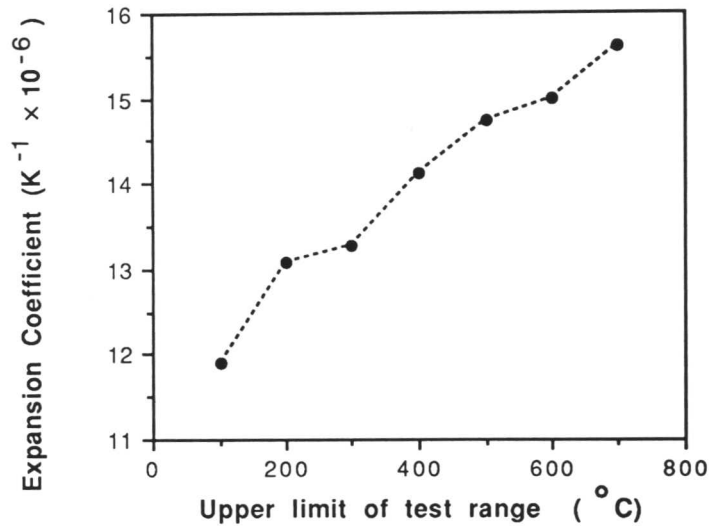


Figure 4.9: Experimentally-determined coefficients of linear thermal expansion for the 1Cr- $\frac{1}{2}$ Mo steam header steel : variation as a function of T_{test} when measured over the range room temperature - T_{test}

proportions of transformed and untransformed regions. This produces an area fraction, which can be considered equivalent to a volume fraction provided the microstructure shows no systematic variation with orientation (if such an orientation relationship did apply, then the area fraction would vary depending on the plane of section and could not be extrapolated with confidence to a volume fraction).

The approach to error analysis which was used for measurements on the as-received microstructure (Gladman & Woodhead, 1960) was used here, giving a 95% confidence limit, $2\sigma_V$, as:

$$2\sigma_V = 2V_v \sqrt{\frac{1 - V_v}{N}} \quad (4.2)$$

The number of readings, N , was selected on this basis to give $2\sigma_V = 0.03$ as the typical uncertainty in the measured volume fraction, which required $N = 400$ – 600 depending on the magnitude of V_v .

The hypothetical dimensions of a 100% ferritic specimen at the transformation temperature can be calculated using the expansion coefficients and the measured length of the rod at ambient temperature. The dilatometer apparatus records specimen length at the start of transformation, when it is 100% austenitic having been fully reaustenitized at 1100°C , and at the end of the run (immediately before quenching to ambient temperature). Now that specimen length for the fully-ferritic, fully-austenitic, and partially-transformed conditions are known, volume fractions of the two phases in the transformed specimen can be calculated, as illustrated by figure 4.10. These results are compared with point counting data in table (4.2) and figure 4.10.

The non-linearity of expansion coefficient with temperature (see above) must be considered: if calculated volume fractions are to be accurate, then a value of expansion coefficient must be appropriate to the isothermal transformation temperature. That is to say, the linear expansion coefficient so used should have been determined experimentally over the range of temperatures ambient – T_{iso} .

4.5.5 Limitations imposed by experimental procedure

The cooling system, although rapid, is not instantaneous. Despite the use of an RF coil heating system (which means that the change in ‘furnace’ temperature is effectively instantaneous), and the helium inert gas quench, the cooling profile during the transition from T_{reaus} to T_{iso} tended to have a form such as that illustrated in figure 4.12, with up to 20 seconds elapsing between the start of the cooling from the austenitizing temperature and the achievement of a stable transformation temperature, and an overshoot of 10 – 20°C below the isothermal temperature. Reduction of the former (by increasing the flow of the helium quench gas) only served to increase the latter, which is highly undesirable. This feature of the apparatus makes time at which T_{iso} is reached determinable only

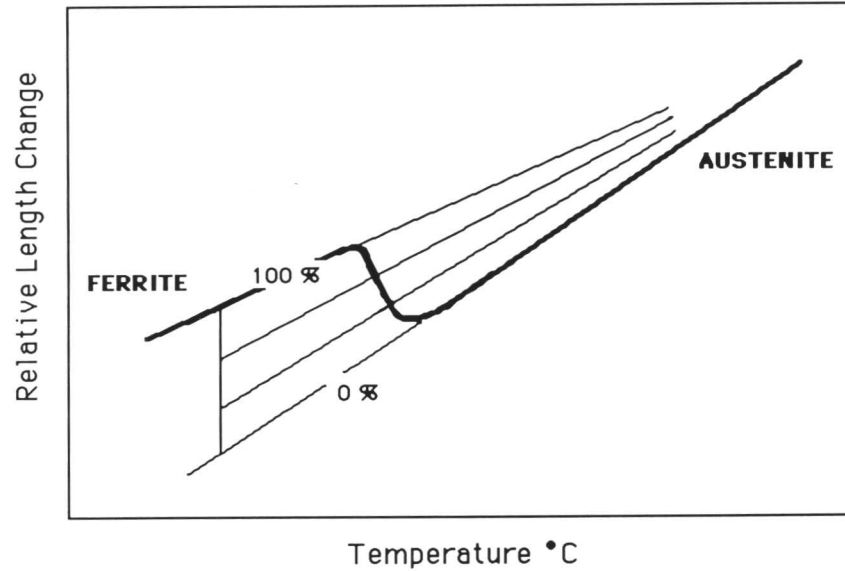


Figure 4.10: Illustration of the procedure followed to determine the volume fraction of the transformed region from dilatometric relative length change vs temperature curves in the 1Cr- $\frac{1}{2}$ Mo power plant steel

to within an accuracy of the order of a couple of seconds, and this is significant at temperatures where the incubation time, τ , is of a similar order of magnitude. Incubation times in the 1Cr- $\frac{1}{2}$ Mo power plant material are predicted to be extremely small at the nose of the upper C curve (around 720°C).

Furthermore, the rapid commencement of the austenite-ferrite transformation in the vicinity of this temperature, coupled with limited cooling rate obtained from the dilatometer in practice, can cause partial transformation to ferrite during cooling through the nose region to isothermal transformation temperatures below 720°C. In this case, the measured incubation times will not be in accordance with theory as the microstructure is already partially ferritic before T_{iso} is reached, which can be expected to retard the onset of the transformation at T_{iso} , so that the measured incubation time is greater than the theoretical τ ,

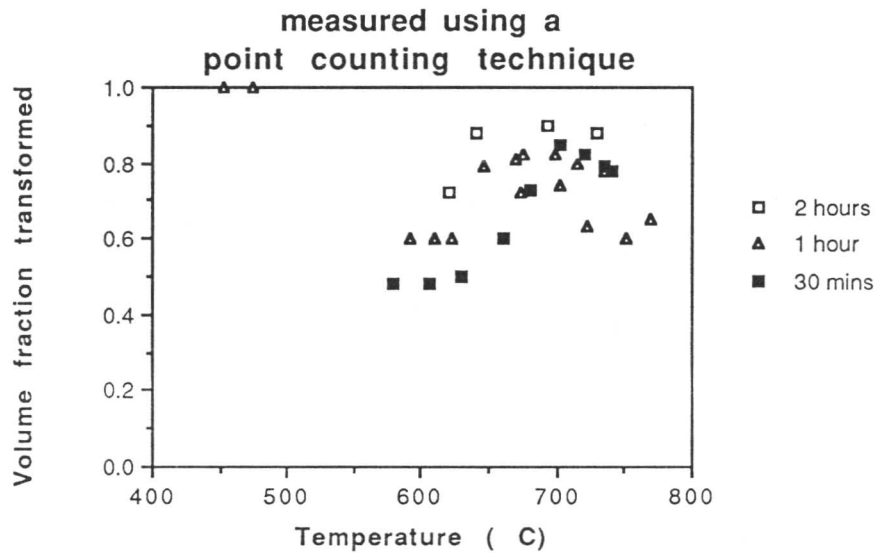
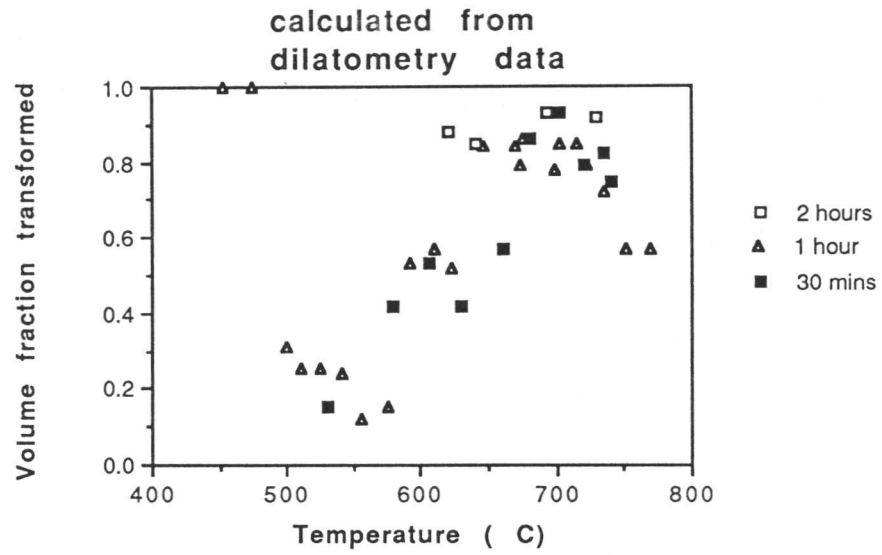


Figure 4.11: Variation of volume fraction of transformed material with transformation temperature for dilatometric experiments on the 1Cr- $\frac{1}{2}$ Mo power plant steel

possibly by an appreciable amount. In any case, it would render the collected data invalid.

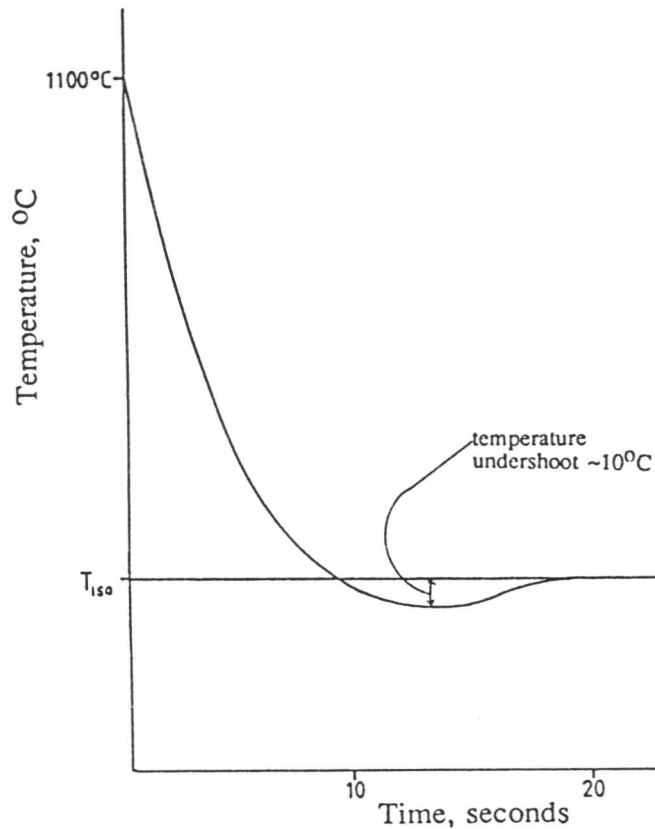


Figure 4.12: Typical cooling curve from austenite to isothermal temperature

It is essential to examine a plot of length vs temperature (figure 4.13) to determine that cooling rates are adequate to avoid this difficulty. These plots should be essentially linear in nature as the specimen is cooled towards T_{iso} if the length contraction is entirely due to the thermal contraction of austenite: a deviation from linearity would be attributable to the transformation volume change occurring during cooling, making the heat treatment invalid.

Examples of the plots used for this purpose are presented in figure 4.13. It is noticeable that in the second case (at an isothermal temperature of 535°C) deviation from linearity (*i.e.*, deviation from the case where only the thermal contraction of austenite is being observed) has occurred before t_{iso} is reached,

whereas the transformation at 720°C exhibits no such problem. This is suggestive of the volume increase associated with the transition from austenite to ferrite having taken place to some extent during cooling in the former case. Included in figure 4.13 is a plot to illustrate that the undershoot of T_{iso} during cooling, which was found to be an inevitable feature of the apparatus, does not necessarily render the result invalid (the transformation run at 700°C, where the absence of any deviation from a linear plot except at T_{iso} confirms that the results produced during this experimental run should be acceptable). The transformation runs where conclusive evidence for prior reaction was found from length change–time plots must be discarded as the experiments failed to produce truly isothermal conditions, but all results where the length vs temperature plots were linear during cooling should be genuinely representative, and are included in table (4.2).

The suspicion that prior transformation may be taking place in some cases was investigated by repeating the isothermal transformations over short time periods for some temperatures. The transformation time was chosen so as to be intermediate between the theoretically-predicted and dilatometrically-measured reaction incubation times, and the material was given a rapid quench. The presence of small colonies of allotriomorphic ferrite within the martensite (figure 4.14) provides confirmation that transformation took place before the measured incubation time, presumably during cooling to T_{iso} through around 720°C where α formation occurs at its most rapid rate. As a consequence, the transformation proceeds more slowly once the desired temperature is reached, and the apparent incubation time is invalid.

The solution to this problem could be to increase the rate of cooling from austenite to the isothermal temperature by using hollow specimens to which a helium line can be attached directly; helium passed through the specimen in this way will produce a much more efficient quench than the method of simply flooding the vacuum chamber. Unfortunately, such a procedure increases the specimen surface area, and hence the risk of surface nucleation effects creating spurious results, as the nickel plating procedure is not perfectly efficient

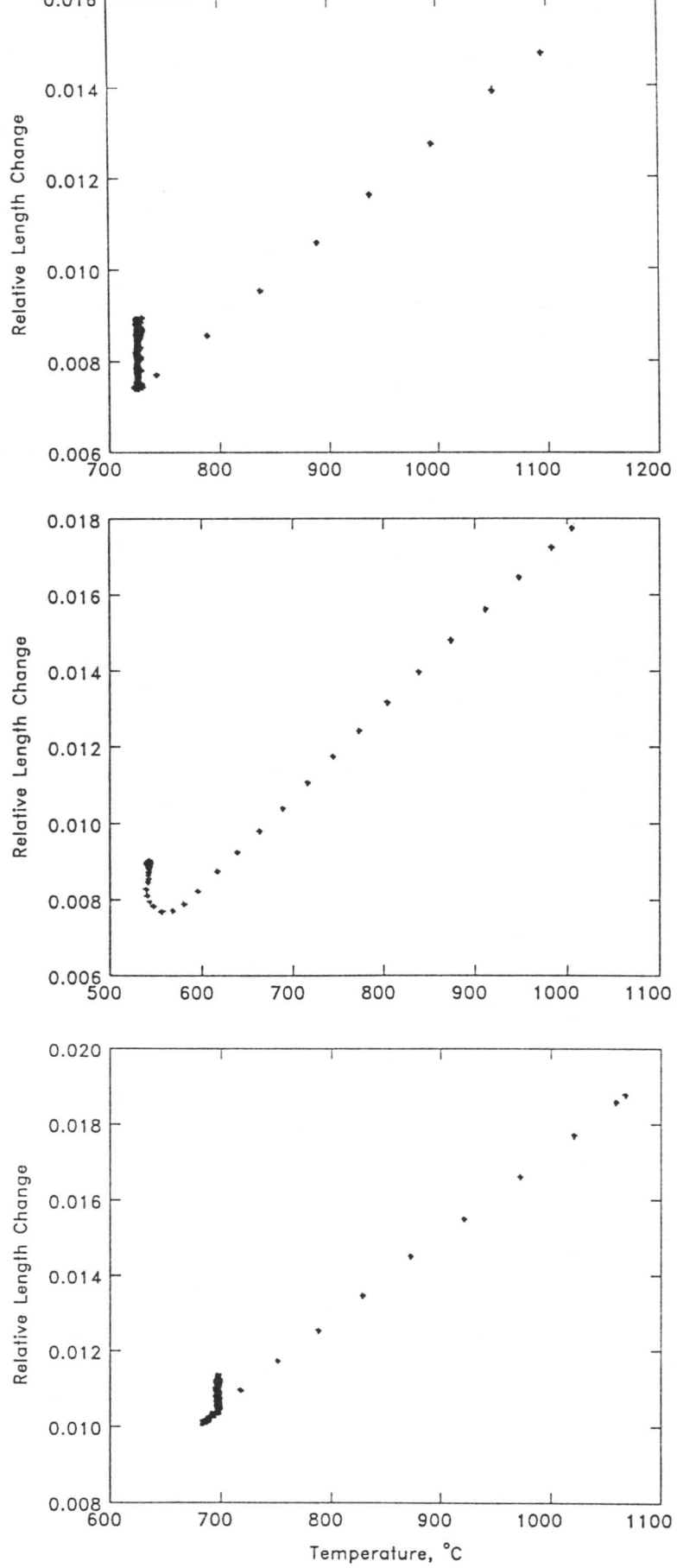
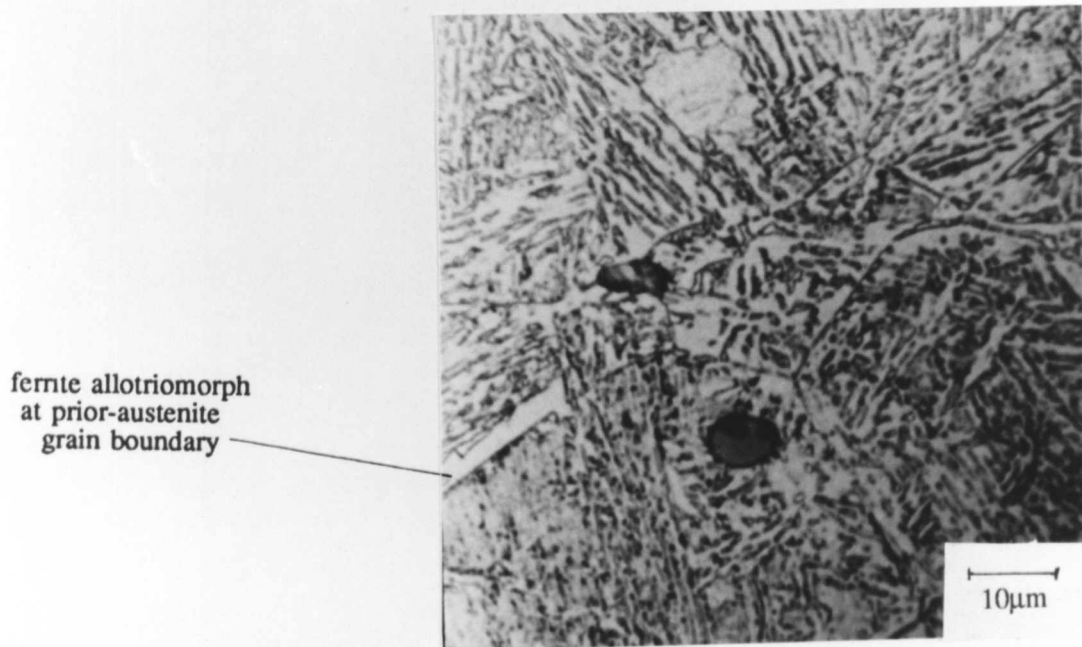


Figure 4.13: Length versus temperature plots for 1Cr- $\frac{1}{2}$ Mo steel isothermal heat treatments



ferrite allotriomorph
at prior-austenite
grain boundary

Figure 4.14: Evidence of initiation of transformation to ferrite during cooling to T_{iso} , negating the validity of the value for τ subsequently calculated from dilatometric data collected at the isothermal temperature

at preventing this, especially on internal surfaces. If such a modification is not practicable, an alternative method such as using a molten-tin bath quench could be employed, although this is less desirable as the excellent data collection facilities provided by the dilatometer would be lost. In this study, the procedure followed has been to vary the rate of helium quenching to try to produce the maximum cooling rate which retains a reasonably clean stop at the isothermal temperature, and to abort those runs which do not achieve this. This approach appears to have proved satisfactory.

4.5.6 A comparison of experimental and theoretical TTT curves

The results obtained from dilatometric data (see table (4.2)) are used to construct an experimental isothermal TTT curve (figure 4.15). It is clear that whilst some points on the graph illustrate good agreement with the theoretical TTT curve generated using Russel's equations, in some cases the fit is poor, especially at isothermal transformation temperatures lying above the nose of the upper C curve. The consideration of the limitations and errors associated with the dilatometric technique has been made above, and some of the factors noted in that section may be responsible for some of this lack of agreement. In essence, the cooling rate available in the system is insufficient entirely to eliminate a suspicion of some transformation occurring before T_{iso} is reached, but on the whole theoretical and experimental values of τ are reasonably close.

An attempt was made to construct a TTT curve based on the experimental incubation times, and this is presented in figure 4.16. This curve, however, does not represent a best-fit through the measured values for τ , but was subject to certain constraints to give the final form a degree of physical significance: the regions above and below the kinetic bainite start temperature were considered separately, and curves fitted to both sets of points; and the upper curve was forced to be asymptotic to the Ae'_3 curve, and was further constrained to take on the familiar C-curve shape. Within these constraints, best-fit splined curves were drawn through both sets of points, and combined to produce figure 4.16. These somewhat arbitrary limits were found to be necessary to produce a curve of meaningful form, but, in consequence, the TTT curve produced in figure 4.16

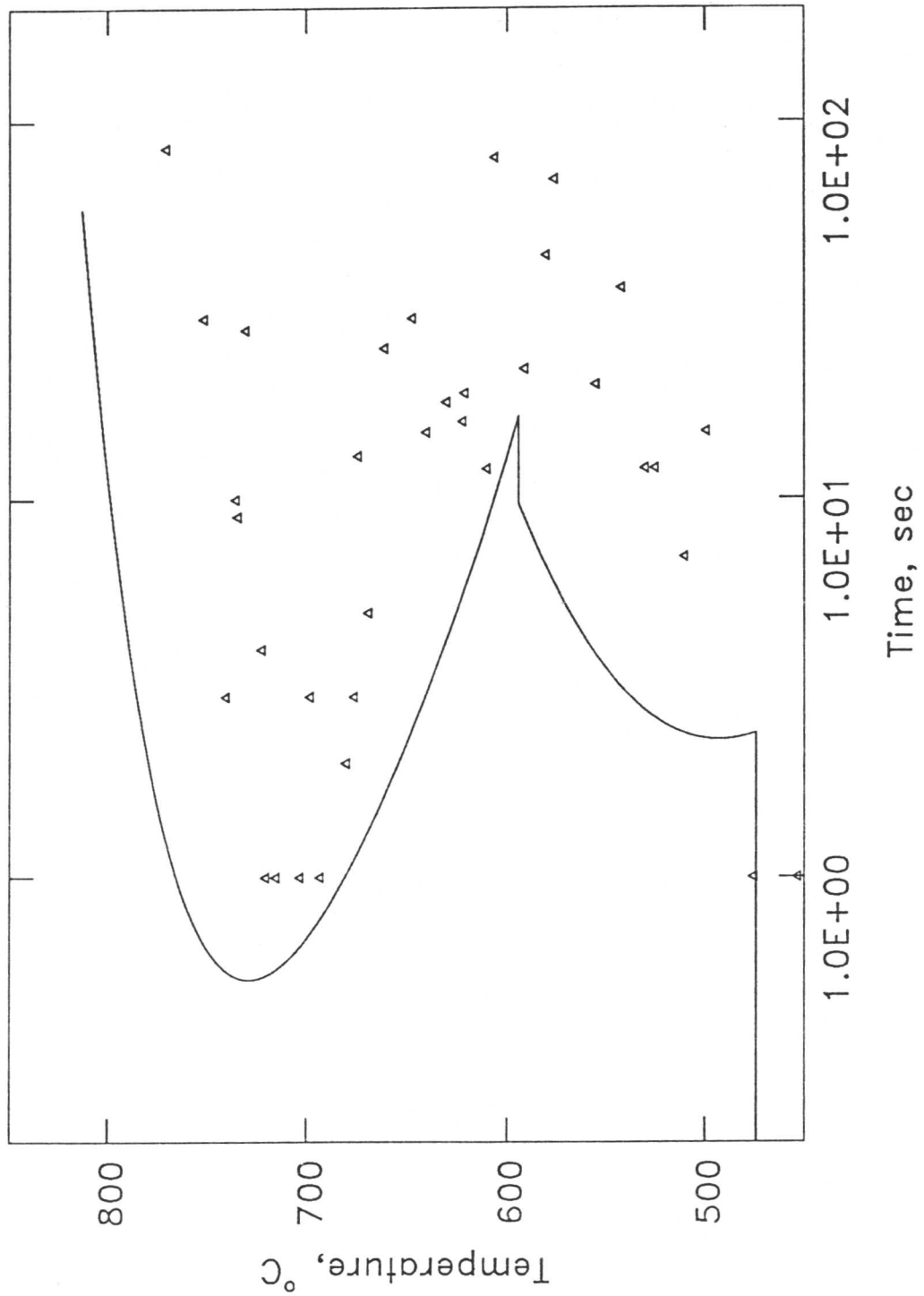


Figure 4.15: Experimentally-determined values for incubation time in comparison with the theoretically-determined TTT curve for the 1Cr- $\frac{1}{2}$ Mo type steam header steel

cannot be said to be a true representation of the experimental data, but rather an approximate illustration of the physical significance of those data.

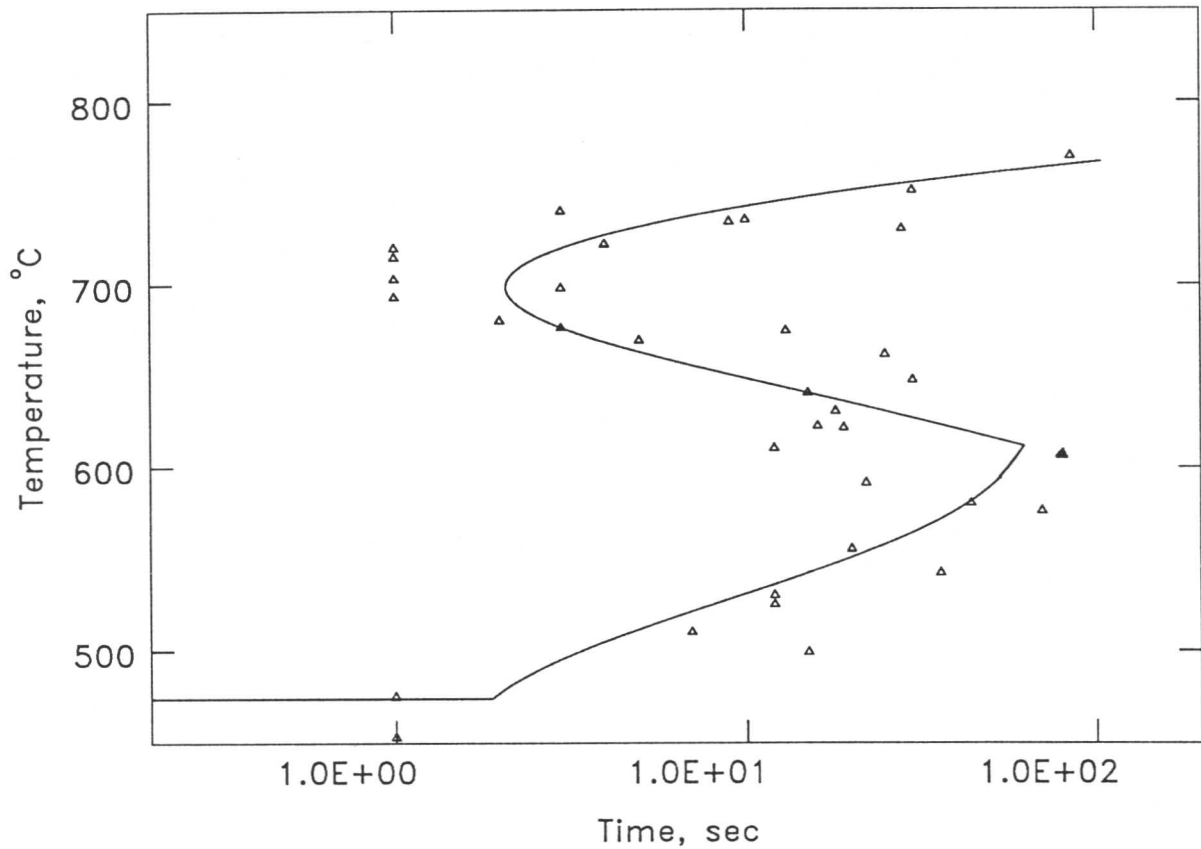


Figure 4.16: TTT curve for 1Cr- $\frac{1}{2}$ Mo type steam header steel determined from experimental data

The TTT curve constructed to represent measured τ is compared with that constructed using Russell's equations in figure 4.17, and shows reasonable agreement with the theoretical prediction.

It may be observed on the graphs that there is particularly noticeable deviation from the theoretically-constructed curve above 720°C. At this temperature, transformation during cooling is unlikely (except in the case of a large temperature undershoot). However, Bhadeshia's program is based on nucleation equations derived by Russell (1969) which are known to be of dubious accuracy for small reaction driving forces and longer incubation times. This is in

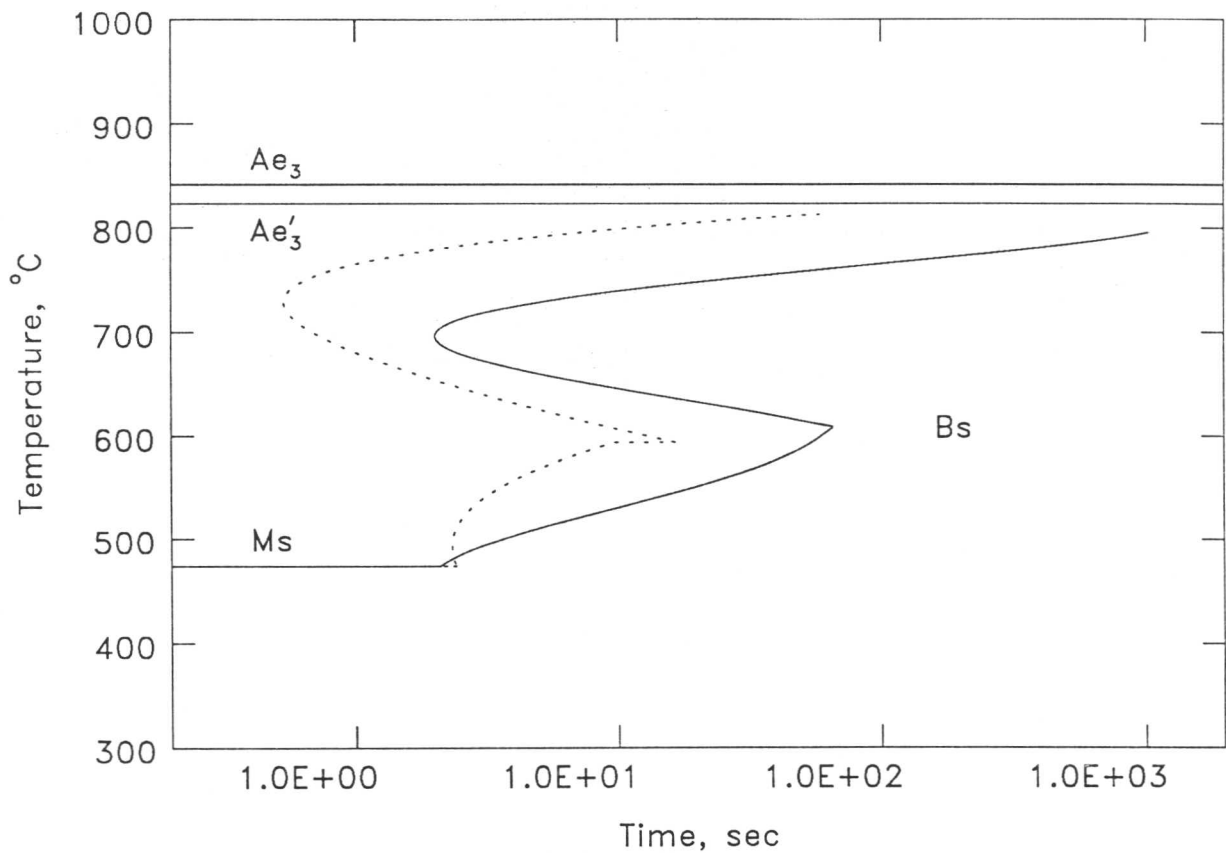


Figure 4.17: A comparison between TTT curves constructed from dilatometric data and calculations based on Russell's equations for the 1Cr- $\frac{1}{2}$ Mo type steam header steel

keeping with the fact that experimental incubation times are consistently longer than those generated by the computer model in the region above 720°C, where Russell's equations cannot rigorously be applied.

4.6 Metallographic Examination of Heat Treated Specimens

4.6.1 Microscopy

The specimens which were prepared of samples from the full range of isothermal transformation temperatures and times, and employed for point counting volume fraction measurement (above), were also examined optically. This was done using an Olympus reflected light microscope, with Ilford FP4 (100 ASA) film used to record the observations. A selection of optical micrographs is pre-

sented in figure 4.18, illustrating the range of transformation products from allotriomorphic ferrite, through bainite, to martensite.

It is notable that on an optical scale is that there was an absence of carbide precipitation within the ferrite of the kind which had been present in the as-received steam header material. In these materials optical evidence for such particles is rarely seen until appreciable ageing has occurred to allow coarsening, or, at the very least, the stress relief heat treatment which is given to pre-service steam header components; hence, any precipitates which would be present in the transformed specimen would be of such a fine scale as to be beyond optical resolution, if present at all.

It can be seen from the micrographs that these microstructures are not always straightforward in interpretation, particularly in relation to the eventual product of the residual austenite which remained after completion of the isothermal transformation run. It can be seen from micrographs obtained from specimens transformed at the higher isothermal temperatures (where the bulk of the material had transformed to allotriomorphic ferrite) that the residual austenite has subsequently decomposed to a mixture of bainite and martensite. This is a consequence of the fact that specimens were air cooled after isothermal transformation (that is to say, at the end of the isothermal transformation the vacuum chamber of the dilatometer was simply opened to air), giving a moderately slow cooling rate; hence some bainite formation was possible from the untransformed austenite before M_s was reached. Lower temperature bainitic microstructures were particularly difficult to analyse: the remaining austenitic regions after transformation could be found as a mixed microstructure of bainite, martensite and even retained austenite (given sufficiently high carbon enrichment of the untransformed region during bainite formation), products which are practically indistinguishable optically, in any case indistinguishable with accuracy. Optical determination of volume fraction transformed was then impracticable for the bainitic microstructures; consequently, measured volume fractions are not presented for this temperature regime in the table of results.

4.6.2 Energy-dispersive X-ray analysis

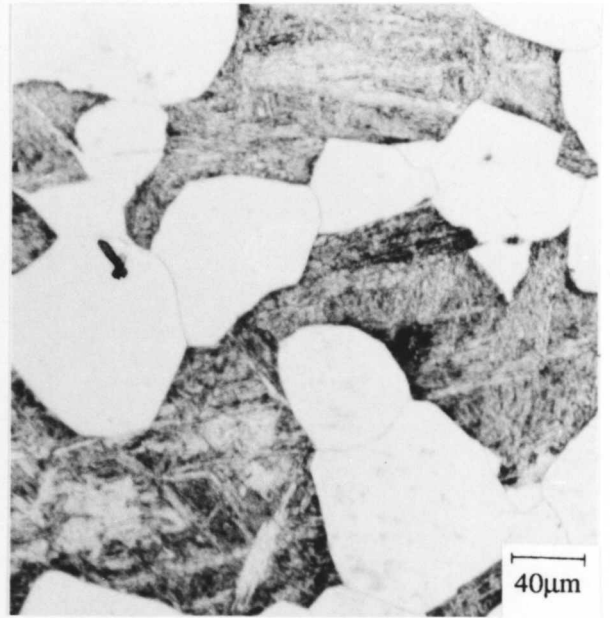
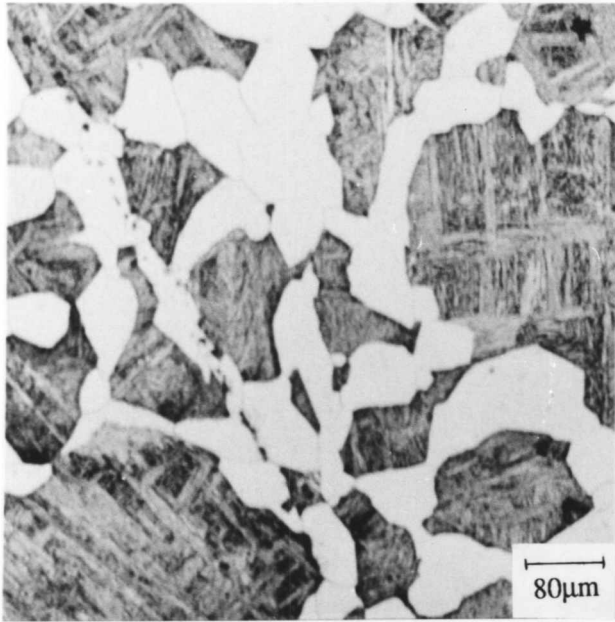
EDX traces were obtained for chromium, manganese, molybdenum and silicon contents for both transformed and untransformed regions in the heat treated steel. The EDX analysis was performed on the ISI100 scanning electron microscope, using the same procedure as for the as-received steam header material, so that results could be compared; they are represented on 4.19.

The figure shows a small difference in composition between allotriomorphic ferrite and martensite with respect to substitutional alloying elements at the highest transformation temperature. In this respect, it shows a similarity to the as-received material, which had also been heat treated at a relatively high temperature (Appendix). Such an effect indicates some redistribution of substitutional alloying elements during transformation at the higher transformation temperature from ferrite to retained austenite (from which the martensite forms on cooling). The scatter in results for a given material is large, however probably due to the large sampling volume (figure 3.14) resulting, in some cases, in a compositional reading being obtained in part from a phase other than the desired one; the accuracy of the data is correspondingly limited, and insufficient for the results to be considered to provide conclusive evidence of redistribution during transformation.

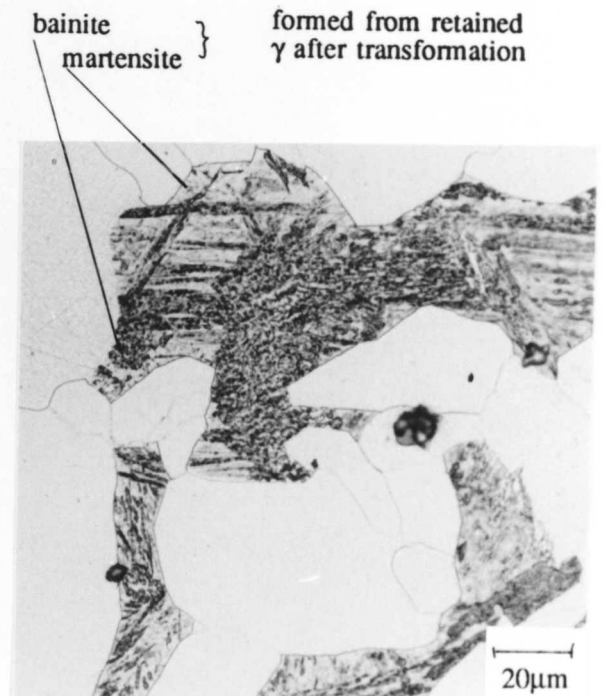
At lower isothermal transformation temperatures, there is no evidence of a difference in substitutional alloying element concentrations between the ferrite and retained austenite, suggestive of a paraequilibrium mechanism for ferrite formation at these temperatures which would be consistent with expectations as undercooling is increased.

4.7 Summary

The austenite–ferrite transformation in the $1\text{Cr}-\frac{1}{2}\text{Mo}$ type steam header steel has been examined carefully using both dilatometric experiments and predictive theory. The transformation behaviour was found to be typical of that expected for a low-alloy, low-carbon steel, producing allotriomorphic ferrite, bainite, and martensite depending on the degree of undercooling from the austenite phase

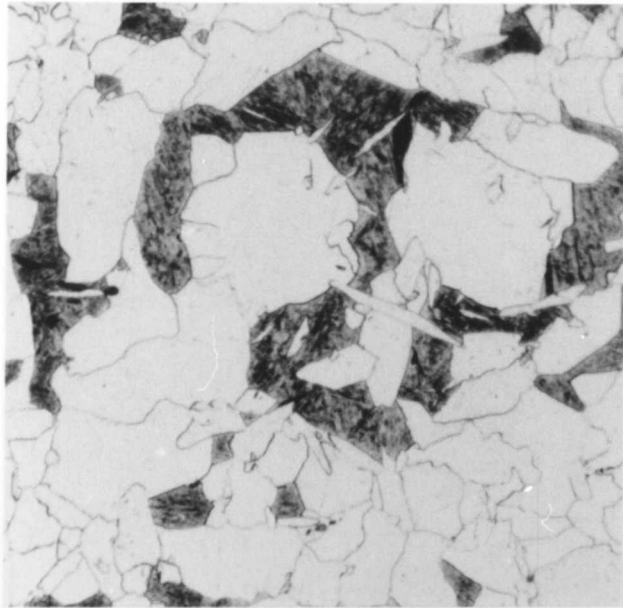


(a) 1 hour @ 750°C



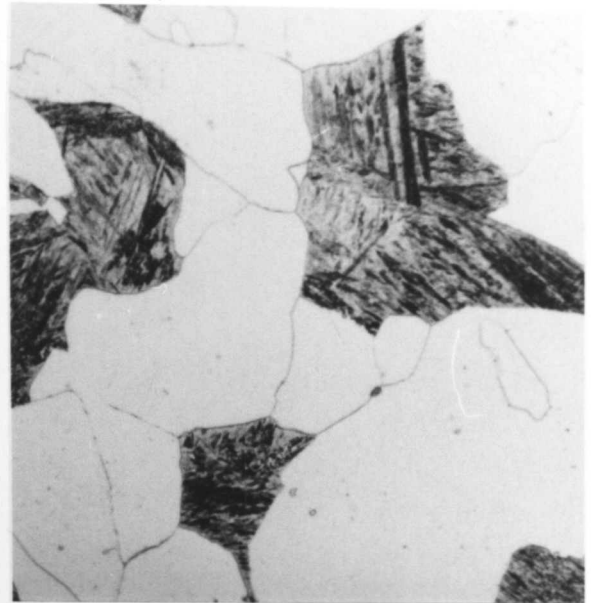
(b) 30 minutes @ 735°C

Figure 4.18 (a) Optical micrographs of heat treated steels



(c) 30 minutes @ 720°C

40µm



20µm



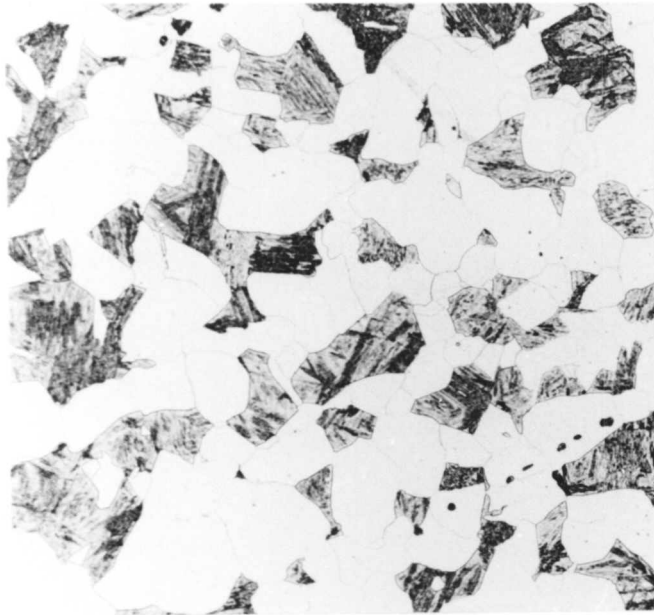
(d) 1 hour @ 700°C

40µm



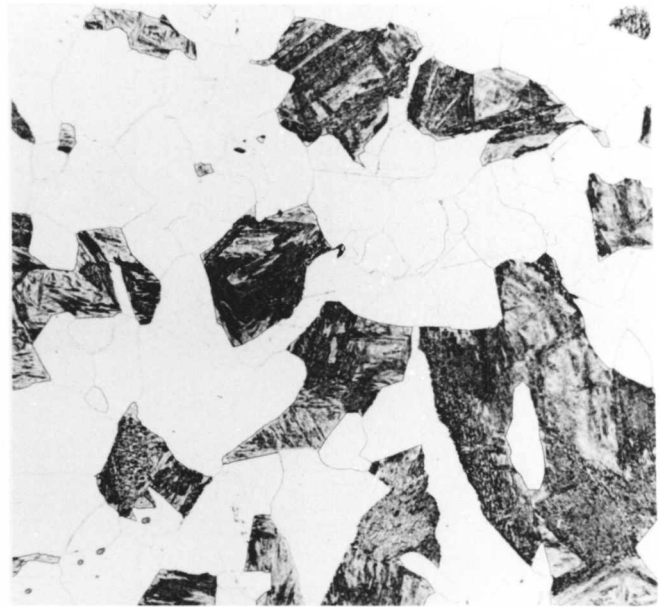
20µm

Figure 4.18 (b) Optical micrographs of heat treated steels

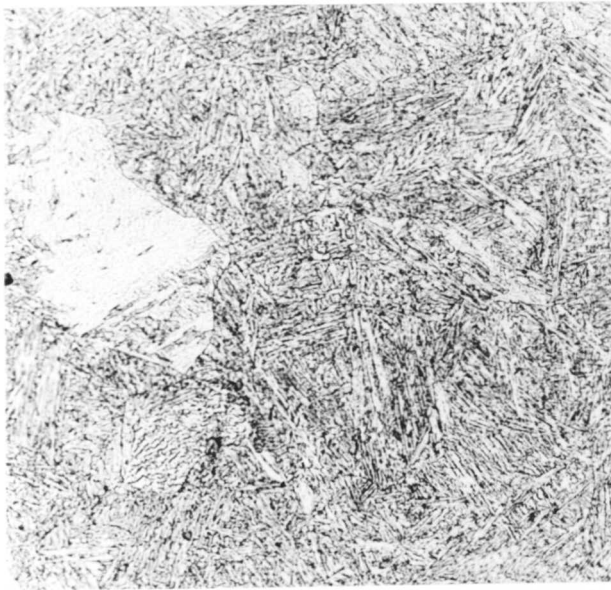


(e) 1 hour @ 650°C

40μm



20μm



(f) 1 hour @ 550°C

40μm



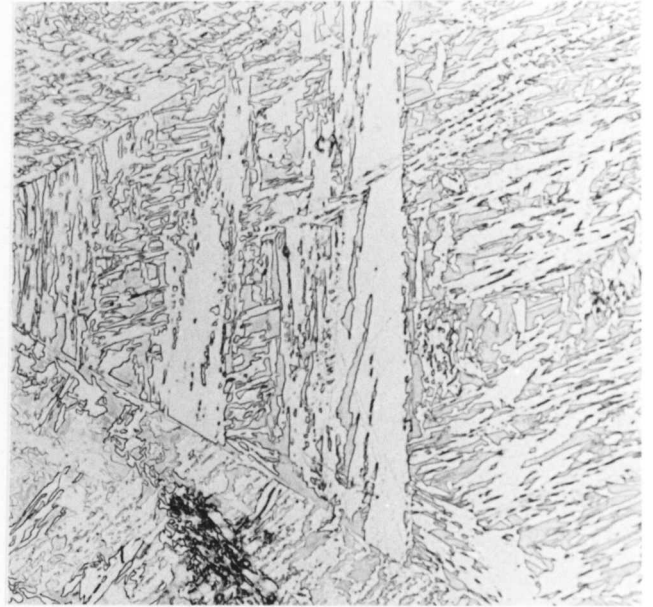
20μm

Figure 4.18 (c) Optical micrographs of heat treated steels



(g) 1 hour @ 500°C

40μm



20μm

Figure 4.18 (d) Optical micrographs of heat treated steels

field. The theoretical modelling of the transformation was also carried out using the composition of the Fe–4.08Cr–0.3C (wt.%) model alloy.

An experimental TTT curve for the transformation has been constructed, and was found to show the standard, two-C-curve form, with a pronounced bay region at around the bainite start temperature. Measurements of the volume fraction transformed to ferrite at different temperatures for a given time were also made; these were found to be typical for a low-alloy steel, and, in the case of bainitic ferrite, to illustrate the incomplete reaction phenomenon. Coefficients of linear thermal expansion were determined for the material, illustrating the non-linearity of ϵ_α with temperature typical of low-alloy ferritic steels.

The knowledge of the austenite–ferrite transformation in the 1Cr– $\frac{1}{2}$ Mo type steam header steel which was obtained by this work may be used in the production of regenerated bainitic and mixed ferritic/bainitic microstructures for the ageing experiments which are described in subsequent chapters.

HEAT TREATED MATERIAL

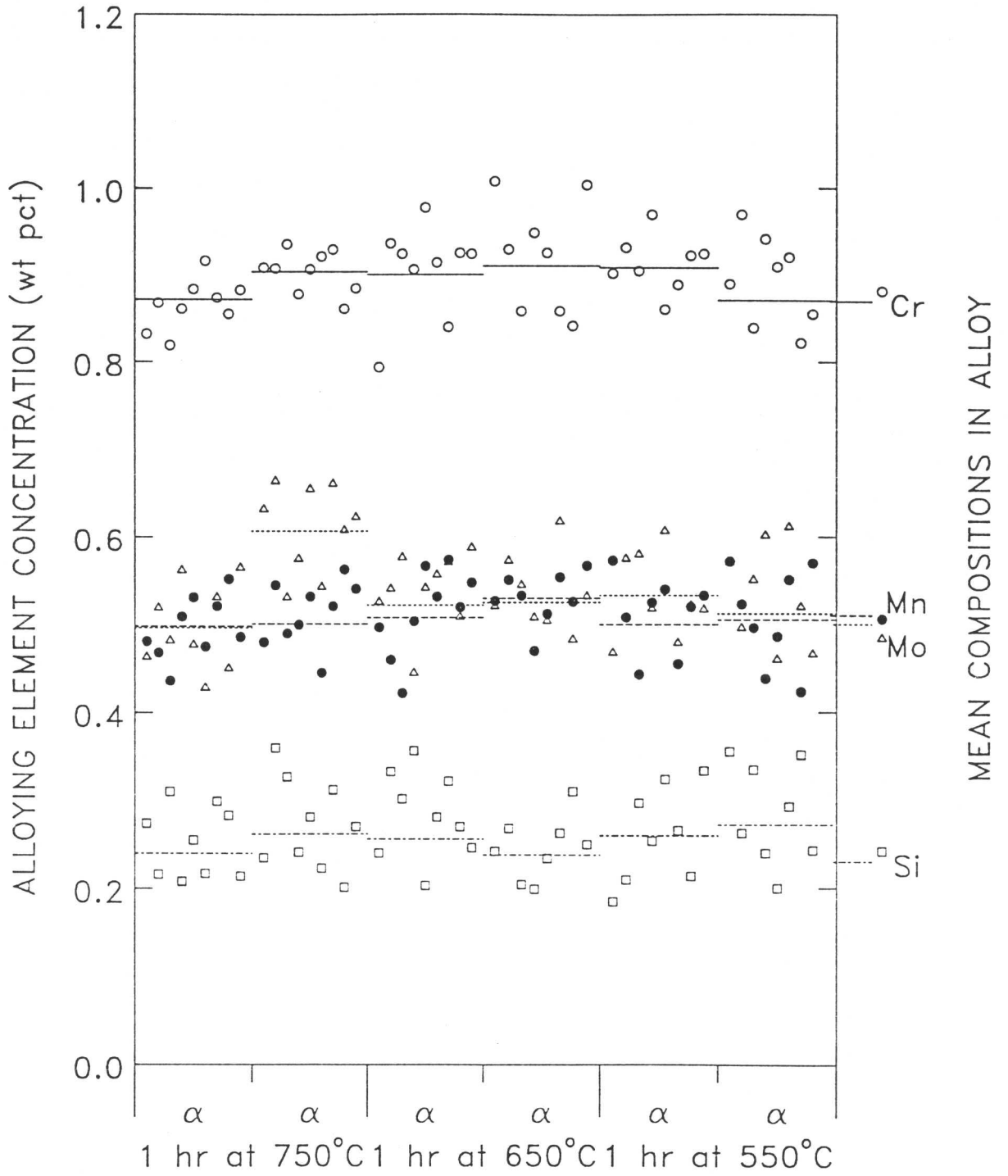


Figure 4.19: EDX results from heat treated steel specimens

Chapter 5

AGEING OF BAINITIC MICROSTRUCTURES: EXPERIMENTAL PROCEDURE

5.1 Introduction

An extensive programme involving the ageing of bainitic and mixed allotriomorphic ferrite / bainite microstructures has been carried out. Specimens have been aged over several temperatures over a range of $\sim 50^\circ\text{C}$ either side of the fossil fuelled boiler system service temperature (*i.e.*, 565°C). The aged specimens have been studied in order to determine the effect of the ageing treatment on their composition (with particular reference to the theoretical model for ageing of θ which was discussed in Chapter 2), microstructure and physical properties. The experimental procedure involved is outlined below.

5.2 Programme of Heat Treatments

Two materials were used with the following compositions (wt. %):

	C	Si	Mn	Cr	Mo	Fe
1	0.30	0.00	0.00	4.08	0.00	bal.
2	0.12	0.23	0.51	0.87	0.50	bal. ¹

Steel 1 was chosen as a model ternary alloy to give an initially simple system of cementite so that the technique could be developed and the theory tested in a controlled manner. Steel 2 is a power plant material and can be expected to give a more complex, and more typically realistic, system of various alloy carbides as well as cementite.

For the second steel (the power plant material), two microstructures have been produced: fully bainitic and a mixture of allotriomorphic ferrite and approx. 25% bainite. The latter microstructure corresponds to that generally observed in actual power plant materials, and will be produced by reference to the

¹ With the exception of negligible levels of sulphur and phosphorus, details of which can be found in the appendix

transformation modelling work which was described earlier. It differs from the as-received material in that it has not been given a subsequent stress-relieving heat treatment following transformation, as it is the intention of the current work to investigate the enrichment of cementite from a precisely known starting composition in order to test recent theory. It is established that bainitic cementite forms with negligible redistribution of substitutional alloying elements, so that it has an initial composition, c_0^θ , which is accurately known; however, the stress-relief heat treatment would introduce significant ageing, so that c_0^θ for the subsequent lower-temperature ageing treatments would not be known so precisely.

5.2.1 Generation of model microstructures

In the case of steel 1, the microstructure was generated by austenitizing at 1100°C for 10 minutes, followed by isothermal transformation to lower bainite at 420°C for 10 minutes. A bainitic microstructure from steel 2 was also generated isothermally, in this case transformed at 530°C for 1 hour. As was noted earlier, the absence of partitioning of substitutionals during bainite formation means that bainitic cementite can be assumed to have substitutional alloy concentrations in the same ratio as those in the alloy as a whole, with a stoichiometric carbon concentration.

The mixed microstructure was generated by performing a partial isothermal transformation at 720°C for 30 minutes, followed by an isothermal treatment of 1 hour at 500°C to transform the remaining austenite to bainite. The temperature of the first half of the treatment was chosen on the basis of the dilatometry in the current work modelling the $\gamma \rightarrow \alpha$ transformation which suggested that such a treatment would produce around 75% transformation to allotriomorphic ferrite. The actual quantity of bainite was measured using a point counting technique with approximately 2000 readings taken, which produced a volume fraction for bainite of $29.1 \pm 1.0\%$ (error is a 95% confidence limit derived using the same procedure as previously).

It was also felt that the undercooling would be sufficient to ensure that the ferrite formed via a paraE mechanism, so that, with no partitioning of substitu-

tionals, the substitutional composition of the retained austenite and transformed ferrite would both be \bar{c} . Thence, as bainitic cementite forms from remaining austenite with no diffusion of substitutionals, it should be safe to assume that the substitutional cementite contents are as \bar{c} , with a stoichiometric carbon concentration. This supposition was confirmed by EDX analysis of cementite particles in unaged specimens, which produced mean compositions of \bar{c} .

Heat treatments were carried out in a fluidized bed set to the isothermal transformation temperature. This method produces a reasonably rapid transition from the austenitizing to the isothermal temperature. The material was sealed in quartz tubes under an appropriate partial pressure of argon to maintain an inert atmosphere at the surface. The temperature must be monitored carefully at the exact point at which the transforming material is placed, to guard against any fluctuations of temperature with distance within the fluidized bed system.

5.2.2 Ageing procedure

The fully-bainitic microstructures were aged at 510°C, 565°C and 625°C, and the partially-bainitic microstructure generated from the power plant steel was aged at 565°C to compare with the fully-bainitic one, giving a total of 7 series of heat treatments. Specimens consisted mostly of 3mm diameter machined rods of approximately 3cm in length. These could then be used both as a source for thin foil work, and for mounting for optical examination and replica production. Ageing was carried out with the specimens sealed in quartz tubes with an inert argon atmosphere.

Material was removed from the furnace at periodic intervals for ageing times of up to a year (*i.e.*, approx 8000 hours).

A careful analysis of the stability of furnace temperature was made in order to obtain a measure of potential experimental error which could be introduced from this source. This involved measuring the furnace temperature at intervals over a period of time, using a Pt-Pt-10%Rh bimetallic thermocouple. The results are represented graphically on figure 5.1.

onto a specimen produced in a manner similar to the procedure described above for optical metallography. The aged material is mounted in acrylic, polished down to 0.25 micron diamond paste, and then given a very light etch in 2% nital to expose the carbide particles. This primary etch should be barely visible optically.

The specimen thus prepared is then placed in a carbon evaporator (see schematic of figure 5.2). The evaporator chamber is evacuated down to a maximum of 2×10^{-4} torr. Resistance heating of high-purity graphite rods is used to evaporate off carbon, which is then deposited onto the specimen below in the form of an amorphous carbon film. The heating effect is achieved by ensuring that one of the rods narrows to less than 1mm in diameter at the point of contact with the other (which has a flat surface) (see figure 5.2). Contact is maintained as carbon evaporates by applying a light force to the narrow-ended rod provided by the spring loading system. It is important to ensure that the surface of the mounted specimen is clean and free from grease to ensure good adhesion of the deposited carbon. This is achieved by washing the specimen in industrial methylated spirits (IMS) immediately prior to insertion into the vacuum system. Carbon is deposited from a height of 10 cm directly above the specimen surface to obtain as even a coverage as possible.

The depth of the layer of carbon is gauged roughly by its apparent colour, which is due to interference effects. As an aid to determining this clearly, a glass microscope slide covering a piece of paper, and with an oil drop on it was placed alongside the specimen. The depth of deposit was judged by comparing the part of the slide under the drop (hence without a carbon deposit) with the rest of the slide.

The carbon layer is found to adhere to those carbide particles which were exposed by the initial light etch. It can thus be loosened from the specimen surface by etching away the ferrite matrix, and hence be removed with the carbides still attached, but without any of the ferrite matrix.

The agent used to etch the replica free from the specimen surface was 10% nital. The specimen was scored with a razor blade into squares around 2mm

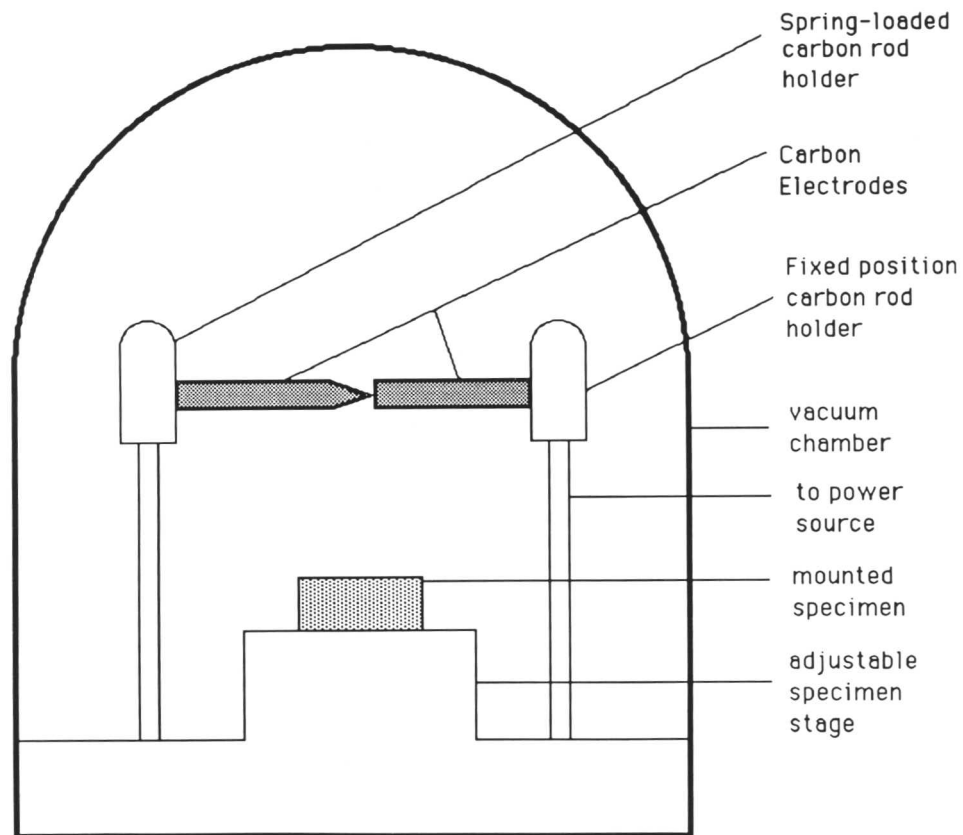


Figure 5.2: Schematic diagram of the carbon evaporator apparatus

across to allow reasonable access for the etchant to bare metal surface, and to ensure that the carbon replica pieces would be of manageable size. The specimen was then placed in the nital and the etching process speeded up by making the specimen cathodic with a 3V potential difference across it.

As soon as the carbon layer had worked almost free of the metal surface, the specimen was washed in ethanol, and the fragments of carbon layer were floated clear of the surface using the surface tension provided by a 50% ethanol / 50% distilled water mixture. It was found that the use of just distilled water for this purpose, as some authorities report, gave too pronounced a surface tension effect, leading to folding over of the replica which was then rendered useless.

Each replica was then collected onto a 3mm, 200 square mesh copper grid and was then ready for analysis in the electron microscope.

5.3.2 The replica technique

The replica technique was chosen because it enables the carbide particles to be analysed in isolation, eliminating any problems which could be caused by interference from signals emanating from the matrix, effects which may be associated with alternative techniques (such as microanalysis of thin foils). This would be a particular problem given the small size of the carbides under analysis. It is likely that the use of thin foils would lead to spurious results, as the spreading and depth of penetration of the EDX beam would mean that a significant part of the spectrum produced would have arisen in the ferrite matrix, and that the compositions extrapolated from the spectra would then be unrepresentative of the actual compositions of the carbides.

These problems can effectively be eliminated by the use of replicas, where no material from the matrix is present, and also the carbon layer is very thin, and hence effectively electron transparent. As a result, the EDX spectrum produced from the replica consists solely of signals from the carbide being tested (with the exception of a very small carbon response and an inevitable background copper signal from the copper grid which can be safely ignored with no loss of accuracy provided copper is not an element under consideration in the carbide analysis). The spectrum can thus be considered to give a true analysis (to within the limits of experimental error and noise) of the composition of the bainitic cementite and other carbide particles under investigation.

5.3.3 Thin foil microscopy

Although the vast majority of this study was conducted using extraction replicas, some thin foils were produced. The primary purpose of examining thin foils was to ensure that the extracted carbides in the replica were representative of the true microstructure. Where necessary, discs were prepared from 3mm diameter cylinders of specimen, initially cut to roughly 0.25mm thick; ground down to 0.05mm on wet 600 grade SiC paper; and jet polished using a twin-jet

electropolisher, with a polishing solution of 5% perchloric acid 25% glycerol (by volume) in ethanol at room temperature, and 40V applied voltage. A Phillips EM400T electron microscope was used for the examination, with an operating accelerating voltage of 120kV.

5.3.4 Procedure for EDX analysis

The replicas were taken and analysed on a Philips 400T transmission electron microscope using the energy-dispersive X-ray analysis (EDX) technique, with 120 kV accelerating voltage, with the specimen orientated at a 30° angle to the detector. The microscope was fitted with a Link EDX analysis system, and the spectra were collected and processed using the Link microanalysis program (which includes corrections for atomic number, absorption and fluorescence effects).

Spurious signals from the system were reduced by using a beryllium specimen holder ($Z = 4$, so the EDX signal from the holder is negligible), although some spurious X-rays arising from the copper grids on which the replicas were mounted could not be eliminated entirely.

Around 30 cementite particles were analysed from each ageing treatment, 'selected' as randomly as reasonably possible from the replica. This number of analyses was found to give data of reasonable statistical significance except at very short ageing times. In each case the EDX spectrum was collected over a 200 s livetime. Micrographs were also taken for each particle from which a spectrum was obtained so that a measure of size could be made.

Diffraction patterns were obtained in order to check that only cementite was being analysed, and to identify any other alloy carbides which may appear after longer ageing times.

5.3.5 Measurement of x_θ

To test a model for the ageing process, such as that producing equation (2.9), it is necessary to obtain a representative indication of particle thickness for each precipitate. For this purpose, a mean linear intercept, \bar{L} was measured from each micrograph.

The mean linear intercept measurement was obtained manually from the appropriate TEM plate. This was done by using a computer program to generate a graph consisting of a random array of straight lines, which was then laid across the TEM plate. The lengths of the various intercepts thus created could be read off to produce a mean linear intercept. A statistical standard error analysis led to the conclusion that around 20 intercepts gave a reasonably accurate value for each mean linear intercept value, with a 95% confidence limit in the measured \bar{L} of the order of $\pm 0.15\text{--}0.20\mu\text{m}$.

It was felt that the mean linear intercept provided the most appropriate measure of the effective mean diffusion length in the cementite particle. The x_θ value in the theoretical model which assumes a cementite slab of infinite length and constant thickness, will thus be best represented by the measured value for \bar{L} in any subsequent analysis.

5.4 Interpretation of Microanalytical Data

5.4.1 Statistical Analysis of Data

Data interpretation involves performing regression analyses to test the correlation of the collected data to several of the predictions which can be deduced from equation (2.9):

- (i) $(c - \bar{c})$ proportional to $1/x_\theta$ at constant t ;
- (ii) $(c - \bar{c})$ proportional to $(\text{time})^{1/2}$ for constant x_θ ;
- (iii) $(c - \bar{c})(x_\theta)$ proportional to $(\text{time})^{1/2}$.

The last two were also tested against the $(\text{time})^{1/3}$ relationship proposed by Afrouz *et al.* (1983) for purposes of comparison.

The best fit $(c - \bar{c})$ v. x_θ^{-1} was also generated in the regression analysis and a statistical significance test performed on the data. This test consisted of fitting the regression coefficient (*i.e.*, the gradient of the best fit line) against the null hypothesis that the true gradient was zero (*i.e.*, no size effect), using a

statistical standard a t-distribution. The t-value thus generated was compared with statistical tables to determine the appropriate confidence limit.

The above statistical analyses were carried out using a computer program for multiple regression analysis using a subroutine from the Numerical Algorithms Group (NAG) numerical analysis package to generate the values for the Pearson product-moment correlation coefficient between x_{θ}^{-1} and $(c - \bar{c})$, and the t-value attributable to the data (and similarly for the $(c - \bar{c})(x_{\theta})$ versus $(\text{time})^{1/2}$ plot). The significance levels quoted in the data presented in the results sections were produced by reading off the t-values produced from the collected data using this procedure and comparing with statistical tables for the t-distribution.

The importance of obtaining a measurement of the statistical significance of any quantitative analysis of analytical electron microscopy, so that results can be processed with reasonable confidence that they are representative, is well documented, e.g. Senior (1988). Senior uses a similar statistical procedure to the one described above in order to determine the sample size required to give significant results. It should be noted, however, that the situation in the quoted reference is not directly analogous to that for the present work,² even though a t-distribution analysis is also used, and the work is referred to primarily as an illustration of the caution required in interpretation of these types of data.

In this work a sample size of about 30 readings per ageing treatment has been used (see above) as this is considered to give tolerable levels of experimental uncertainty in the $(c - \bar{c})$ v. x_{θ}^{-1} analysis, whilst producing plenty of data for the analysis of composition change versus time (a larger sample size would increase the accuracy of the former analysis, but at the expense of the latter). This

² Senior's study consisted of an attempt to quantify the relative proportions of two distinct types of precipitate occurring simultaneously in a microstructure using the EDX technique. The statistical analysis produced a figure for the uncertainty in these measured proportions. In the case of the current project only a single type of particle (*i.e.*, cementite) is analysed, and the level of significance quoted is that associated with the proposed relationship between the composition of various of these particles and an independent variable (*e.g.*, the precipitate size).

sample size is found to produce adequate significance levels for the $(c - \bar{c}) \text{ v. } x_{\theta}^{-1}$ analysis, at least for specimens from longer ageing times (where the size effect becomes reasonably pronounced).

It is also apparent from equation (2.9) that an approximate activation energy for the diffusion process can be determined provided that data is available over a range of temperatures (because most of the temperature dependence of the Bhadeshia model is attributable to D_{α}). These were also determined for each set of heat treatments.

5.4.2 Inaccuracies in EDX measurement due to matrix effects

The essence of the EDX technique lies in the ability to extrapolate relative X-ray signal intensities for two elements within a specimen (say, I_A/I_B) to the relative concentration of the elements present (C_A/C_B), in accordance with equation (5.1), below (Cliff and Lorimer, 1975), where k_{AB} is a constant for constant accelerating voltage and specimen thickness.

$$\frac{C_A}{C_B} = k_{AB} \frac{I_A}{I_B} \quad (5.1)$$

Factors affecting the proportionality between the two are therefore of considerable concern, and care must be taken to quantify and if necessary correct for such factors before the compositional data produced by the technique can be used. Consideration is given to two such problems: unequal level of absorption of different X-ray emissions (from different elements) by the specimen; and fluorescence within the specimen.

5.4.2.1 Absorption

The Link system used in analysing the EDX spectra includes a routine to make a correction for matrix absorption from specimen thickness and density. A brief consideration of the physical situation is given below.

The relationship between the observed intensity of signal from an element A present in the specimen, I'_A , and the real intensity of emission which would

be observed in the absence of any absorption, I_A , follows the exponential law as equation (5.2).

$$I'_A = I_A \exp\{-(\mu/\rho)_{\text{spec}}^A \rho x\} \quad (5.2)$$

where x is the distance the signal travels through the material, ρ is the density of the material, ϕ_A is a measurement of the attenuation of incident electron energy during its passage through the material, and $(\mu/\rho)_{\text{spec}}^A$ is the mass absorption coefficient for X-ray emission attributable to element A for the whole specimen, obtained as a sum over all elements in the specimen of $c_i(\mu/\rho)_i^A$, where c_i and $(\mu/\rho)_i^A$ are the weight fraction and mass absorption coefficient associated with the element i .

In a practical situation for a specimen of finite thickness, d , Goldstein *et al.* (1977) thus propose equation (5.3) for the relationship between I'_A and I_A .

$$\frac{I'_A}{I_A} = \frac{1}{d} \int_0^d \phi_A(\rho x) \exp\{-(\mu/\rho)_{\text{spec}}^A \csc(\psi) \rho x\} dx \quad (5.3)$$

where ψ is the take-off angle, and, for practical purposes, is assumed to fit the relationship

$$\csc(\psi) = \frac{1}{\sin \alpha \cos \theta + \cos \alpha \sin \beta} \quad (5.4)$$

where α is the tilt angle, θ is the angle between the detector and tilt axes, and β is the elevation of the detector, which is zero for Philips instruments such as the one used in the current work.

If it is assumed that the electrons lose negligible energy during passage through the specimen (that is to say, the rate of production of X-ray photons is constant through the thickness d), then $\phi(\rho x) = 1$ (Cliff and Lorimer, 1975). Thus equation (5.3) can then be reduced to equation (5.5). This assumption is generally considered a reasonable approximation in thin films, although for slightly thicker specimens it may break down.

$$\frac{I'_A}{I_A} = \frac{1 - \exp\{-(\mu/\rho)_{\text{spec}}^A \csc(\psi)\rho d\}}{(\mu/\rho)_{\text{spec}}^A \csc(\psi)\rho} \quad (5.5)$$

A correction factor for intensity ratios can then be obtained by combining the above equation with an identical equation for an element B. This approach allows the ratio I_A/I_B to be quantified as equation (5.6), which makes it apparent that the effect of absorption depends on the difference between the mass absorption coefficients for the two elements, as well as on specimen density and thickness.

$$\frac{I_A}{I_B} = \frac{I'_A}{I'_B} \times \frac{(\mu/\rho)_{\text{spec}}^A (1 - \exp\{-(\mu/\rho)_{\text{spec}}^A \csc(\psi)\rho d\})}{(\mu/\rho)_{\text{spec}}^B (1 - \exp\{-(\mu/\rho)_{\text{spec}}^B \csc(\psi)\rho d\})} \quad (5.6)$$

A further approximation has been proposed by Lorimer (1975) assuming a mean path length for an emitted X-ray between absorption events of $d/2$. The use of this approximation simplifies the evaluation of equation (5.3), producing equation (5.7) below.

$$\frac{I'_A}{I_A} = \exp\{-(\mu/\rho)_{\text{spec}}^A \csc(\psi)\rho(d/2)\} \quad (5.7)$$

The use of this further approximation produces the correction factor for observed against true concentrations as in equation (5.8).

$$\frac{I_A}{I_B} = \frac{I'_A}{I'_B} \times \exp\{-[(\mu/\rho)_{\text{spec}}^B - (\mu/\rho)_{\text{spec}}^A] \csc(\psi)\rho(d/2)\} \quad (5.8)$$

The practical problem in quantifying absorption thus becomes one of obtaining reasonable estimates for ρ and d , or alternatively a figure for the combination ρd the “effective mass path length”. The latter approach is easier in

some practical situations, as it may be possible to obtain a value for the effective mass path length directly from the spectra. This is generally done by either comparing K and L lines from a given element of reasonable concentration within the specimen (which requires that the K and L lines have appreciably different absorption behaviour, requiring $Z > 27$ in practice), or taking a series of spectra from the same area at slightly different tilts to produce a series of data with known relative path lengths (which requires a specimen of clearly known geometry). In this project neither approach for the determination of ρd would be practicable, and estimates of density and thickness are made separately.

5.4.2.2 Fluorescence

Fluorescence effects in EDX microanalysis can arise either from the continuum or from a characteristic line. It is generally held that continuum fluorescence is likely to present a serious problem only in bulk samples, and can reasonably be ignored for thin foils, where continuum fluorescence will be sufficiently small to be trivial compared with other sources of error.

In the case of characteristic fluorescence some problems have been reported even for thin foils, notably for $\text{Cr}K_\alpha$ radiation for low chromium concentrations in iron (Lorimer *et al.*, 1977, see figure 5.3). The levels of fluorescence found were smaller than for bulk specimens, but still appreciable at chromium concentrations of below about 10%, with the measured chromium composition being overestimated by a factor of 30% for a chromium concentration of 1%. This result was obtained from a thin foil which Lorimer estimated to have a thickness of around 2000 Å and hence may be of relevance to this work. Lorimer further suggested that, in thin foils, the degree of this effect would vary as $d \log d$, which approximates to d at small values, where d is the specimen thickness.

In order to quantify the problem for the experimental conditions applying in this case, EDX spectra for the as-transformed bainitic microstructure were considered in detail, as it was known that these should have a composition of (\bar{c}) . Measurements made on the 1Cr- $\frac{1}{2}$ Mo type steel were found to give a mean value for chromium composition which exceeded \bar{c} by 0.08 at%, or about 10% of the expected value (see tables 6.1-3), which compares with a statistical

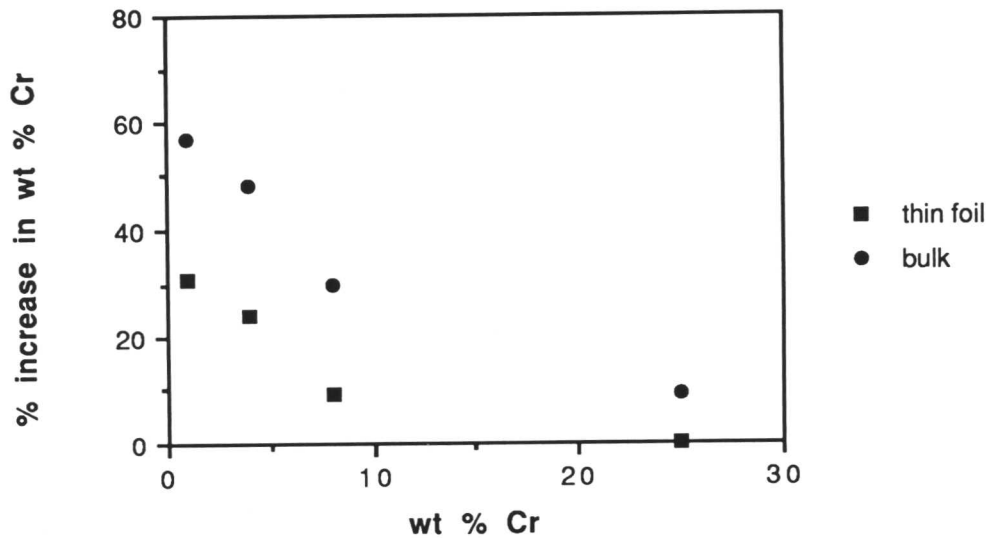


Figure 5.3: Variation in % increase in Cr concentration as a function of Cr concentration for EDX analysis of bulk and thin film specimens (Lorimer *et al.*, 1977)

standard error which was found typically to be of the order of 0.5 at% for these EDX spectra. If Lorimer's relationship for specimen thickness holds, given x_θ which mostly lie between 0.1 and 0.2 μm , then an overestimate attributable to fluorescence for particles of these two sizes can be estimated to be of the order of +0.05 at% and +0.10 at% respectively, a difference which is much less than (and in the reverse direction to) the predicted size effect for all but the shortest ageing times.

In view of the fact that the observed systematic error is relatively small compared with other uncertainties in these EDX measurements, that the effect is exaggerated at small values of c^θ , so accuracy will improve with enrichment during ageing, and that it is difficult to measure x_θ accurately whilst collecting the spectra, it is unlikely that any attempt to allow for this apparent effect will yield a significant improvement in accuracy.

Problems caused by characteristic fluorescence with manganese and molyb-

denum have not been reported, and any such effect can be expected to be trivial in the case of these elements.

5.4.3 Inaccuracies in EDX measurement due to spurious effects

5.4.3.1 Instrumental sources

Spurious X-rays which do not arise from a single event in the specimen by the central electron beam have been attributed to several instrumental factors (Goldstein & Williams, 1978).

- (i) Bremsstrahlung radiation from the condenser apertures and electrons uncollimated by the condenser may generate X-rays from both the specimen and its surroundings.
- (ii) Electrons scattered in the chamber can generate a signal from specimen or surroundings.
- (iii) X-rays can be generated in the specimen or surroundings by electrons scattered from the specimen.
- (iv) X-rays generated within the specimen can cause fluorescence of the surroundings.
- (v) In the case of extraction replicas, X-rays may be produced by the copper grid used to support the specimen.

Effects (ii)–(iv) can be reduced to a trivial level by appropriate experimental practice (consistent electron beam, shielding of the specimen with low-atomic-number materials – hence the beryllium holder – *etc.*). The fifth effect is only a problem if copper is also present in the material (in which case a different grid could be used), otherwise the spurious Cu signal may be safely ignored. However, it is important to maintain vigilance to ensure that these effects do not constitute a serious problem in the collected data.

5.4.3.2 Specimen based sources

Spurious results in EDX analysis have been reported in a number of cases as arising from problems in the specimen. In particular, variation in specimen

thickness is liable to give variable results. This will arise in part because any difficulty in determining an accurate specimen thickness will introduce an error into any estimate of the magnitude of thickness dependent effects (fluorescence and absorption). In addition, it has been suggested that enrichment of one species relative to another in a surface film (such as an oxide layer), will produce further variations of EDX spectra with specimen thickness (Morris, Davies & Treverton, 1977).

Spurious results arising from foreign species at the specimen preparation stage have also been documented (*e.g.*, residues from etching and polishing solutions), emphasizing the need for care in replica preparation: high-purity carbon rods were used as the evaporation source; the optical specimens were scrupulously cleaned before insertion into the evaporator (which is also essential for good carbon film adhesion); and the replicas were thoroughly washed in pure ethanol before the lifting stage (in the ethanol / distilled water solution) to remove etching residues.

5.4.4 Stochastic scatter in EDX measurements

Even when systematic errors in the EDX results, such as could arise from absorption, fluorescence, spurious X-rays *etc.*, have been accounted for, an individual EDX composition will be subject to an error attributable to stochastic scatter in the X-ray signal intensity (both background and characteristic). The EDX spectrum analysis program makes an estimate of this error on the basis of the observed noise in the collected spectrum, enabling the problem to be quantified approximately, and the scatter can be reduced by extending the time period over which the spectrum is collected, to increase the signal : noise ratio.

In practice, the composition which is measured from an EDX spectrum, c_{obs}^{θ} will be related to the actual composition, c_{real}^{θ} , by equation (5.9)

$$c_{\text{obs}}^{\theta} = c_{\text{real}}^{\theta} \pm x \quad (5.9)$$

where x is a factor representative of the stochastic scatter in the observed signal intensity at the characteristic frequency under analysis. The stochastic nature

of the error imposed on individual measurements by this factor means that confidence limits in the measured mean composition for a given ageing time can be increased by the standard expedient of increasing the number of measurements taken from specimens aged to that time (hence, approximately 30 particles were measured at each ageing time in the current work).

It is evident that, where the characteristic-peak intensity is small (for a small concentration of the element concerned), and the noise in the background signal is of a similar order of magnitude, it is possible that the stochastic scatter in c^θ is larger than the magnitude of c^θ , which will produce an occasional negative result for the concentration of the element when the spectrum is analysed. Such a result indicates that the X-ray intensity at the characteristic frequency in that particular spectrum is less than that which would be expected from background radiation alone, as a result of the stochastic noise in the background signal.

A negative value for c^θ is clearly of no physical significance as a composition, and results obtained from specimens where this problem arises must be treated with considerable suspicion; the true composition is so small as to be of a similar order of magnitude to the resolution of the technique. Nevertheless, because such results arise from a random process inherent in the EDX technique, it is necessary that they be included when mean compositions are calculated from a large number of observed c^θ values. In the current work, where substitutional alloying content is relatively small at short ageing times, conditions were set as carefully as possible to reduce the stochastic scatter to a minimum (by ensuring that the error in each reading, which was calculated by the analysis program from the spectrum and was, in effect, an estimate of this scatter, remained small). In consequence, the number of spectra which produced negative values for a composition was kept small, although such results were occasionally obtained, and were retained for analysis for the above reason.

Chapter 6

AGEING OF BAINITIC MICROSTRUCTURES:

Fe–Cr–Mo POWER PLANT STEEL

6.1 EDX Compositional Data

6.1.1 Procedure

The EDX microanalytical data for the series of heat treatments done on the 1Cr– $\frac{1}{2}$ Mo power plant steel were collected and analysed, in accordance with the procedure described in the previous chapter, by comparison with the simple analytical solution of equation (2.9). This equation is used extensively in the following pages, so it is reproduced below, as equation (6.1), for ease of reference:

$$t_c = \frac{\pi[x_\theta(c^\theta - \bar{c})]^2}{16D_\alpha(\bar{c} - c^{\alpha\theta})^2} \quad (6.1)$$

where t_c is the time to reach cementite of concentration c^θ ,

\bar{c} is the mean alloy composition,

x_θ is the cementite particle size,

$c^{\alpha\theta}$ is the composition of α in equilibrium with θ ,

and D_α is the diffusivity in ferrite.

Measurements for particle size and degree of enrichment for a given ageing time are processed by a regression analysis for $(c - \bar{c})$ versus $1/x_\theta$, and the results are presented in table 6.1 for the series of specimens aged at 510°C, in table 6.2 for specimens aged at 565°C, and in table 6.3 for specimens aged at 625°C. In all three cases the initial microstructures had been generated by heat treatments prior to tempering to be fully bainitic. It should be noted that the units used in the table are μm for x_θ (the measured mean linear intercept) and at.% of total

substitutionals¹ for $(c - \bar{c})$, and that the data presented for the best fit produced from the regression procedure will be consequently in similar non-standard units.

6.1.2 Accuracy of EDX data for the elements present

The accuracy of EDX data is found to be dependent, to some extent, on the substitutional element under investigation. The tables of experimental data show relatively better agreement to proportionality of $(c - \bar{c})$ to x_θ^{-1} for chromium and manganese than for molybdenum, especially at shorter ageing times; observed molybdenum compositions are substantively greater than \bar{c} at zero time, and higher than the analytical model predicts after ageing; and nothing of statistical significance is obtained when the regression analysis is performed on the silicon data.

(i) Chromium and manganese

The characteristic K_α peaks for these two elements are well defined, reasonably large, and readily distinguished from signals produced by the other elements present. The equilibrium partition coefficient between cementite and ferrite, $c^{\theta\alpha}/c^{\alpha\theta}$, is much greater than unity in both cases; therefore diffusion in ferrite should be the controlling process, and appreciable enrichment will occur reasonably quickly, making the observed random variations in measured c_0^θ (as-transformed cementite compositions) trivial relative to $(c - \bar{c})$. In consequence, the EDX composition measurements are well representative of real cementite compositions.

(ii) Molybdenum

Molybdenum analysis uses the L peaks, as the energy required to produce K de-excitations is too large. It is well established that the spread of the molybdenum characteristic coupled with its proximity in the spectrum to the sulphur K_α

¹ For much of this work, c^θ is expressed as an atomic percentage of the substitutional elements only, excluding carbon. This facilitates development of models for processes where diffusion only in the substitutional lattice is of concern, and is also in accordance with EDX methods which do not detect carbon. Atomic percentages are used so that conversion to an absolute (*i.e.*, inclusive of carbon) value is done by way of a simple linear relationship, assuming stoichiometric carbon content of cementite.

signal can cause the two to become difficult to distinguish in spectra from steels containing both elements (as did the steel in the current work, see appendix). This could be the cause of the non-zero as-transformed value for $(c - \bar{c})$. Furthermore, the molybdenum peak intensity is appreciably less than those from chromium and manganese (in part because the molybdenum content is lower), resulting in a poorer characteristic-signal to background-continuum-noise ratio which could be detrimental to the accuracy of the determined composition, and the larger atomic number differential between iron and molybdenum than between iron and the other substitutionals would exaggerate any errors inherent in the correction.

It can also be noted that $c^{\theta\alpha}/c^{\alpha\theta}$ is not so large for molybdenum as for chromium and manganese, and that the diffusion coefficient is less; therefore, the enrichment process is slower and any experimental errors which are present will remain significant relative to $(c - \bar{c})$ for longer ageing times.

(iii) Silicon

Silicon differs from the other elements under investigation in that $c^{\theta\alpha}/c^{\alpha\theta}$ is less than unity, so that silicon rapidly passes into ferrite from cementite. Any reading obtained for silicon in cementite will be too small to be experimentally significant given the possible scatter. Consequently, although silicon EDX measured compositions are presented for completeness, the data are of inadequate accuracy for further analysis.

6.2 Variation of Composition Change with Particle Size

Typical examples of sets of compositional measurements for a given heat treatment, plotted against x_{θ}^{-1} in accordance with equation (6.1), are presented in figure 6.1(a)–(e). Each point on these graphs represents the measured composition and size of an individual cementite particle in the aged specimen.

6.2.1 The as-transformed condition

Bainitic carbides are expected to form with negligible partitioning of substitutional alloying elements during transformation (section 2.2). Nevertheless, it is

also noticeable in figure 6.1(a) that in the as-transformed state larger particles appear to show a trend to slightly higher compositions, in contrast to the situation for aged specimens where smaller particles have enriched to a greater degree. Similar trends have been found for the as-transformed specimens in other series in this steel, as is illustrated by figure 6.2.

Where this effect is observed for chromium, it may be attributable to the fluorescence effect noted by Lorimer *et al.*(1977) and discussed in the previous chapter, but similar results are observed for manganese and molybdenum concentrations. A tentative explanation is offered that this effect is due to the fact that the larger particles of cementite formed first, and hence have undergone a little enrichment even at the low transformation temperatures. However, although the effect is plausible, it is very small, and of low statistical significance, and disappears rapidly as soon as the ageing treatments and the associated general enrichment process begin. It would inevitably disappear rapidly, because of the increased enrichment rate of smaller particles relative to larger ones that is predicted by equation (6.1).

6.2.2 Variation as ageing time increases

Rearranging equation (6.1) to give the relationship in equation (6.2), it can be seen that, for a given time, the change in composition of cementite, $(c^\theta - \bar{c}) \propto 1/x_\theta$, the mean linear intercept.

$$(c^\theta - \bar{c}) = \frac{t_c^{1/2}}{x_\theta} \frac{4D_\alpha^{1/2}(c^{\alpha\theta} - \bar{c})}{\pi^{1/2}} \quad (6.2)$$

where $4D_\alpha^{1/2}(c^{\alpha\theta} - \bar{c})/\pi^{1/2}$ is constant for a given material at a fixed temperature.

It is apparent in the data presented in the tables for the $(c - \bar{c}) \text{ v } x_\theta$ that, as the ageing time was increased, the correlation coefficient which is calculated for this predicted size effect (*i.e.*, $(c - \bar{c})$ versus $1/x_\theta$) shows a general improvement with prolonged ageing. The trend is most clearly exhibited by chromium, less so by manganese due to the lower degree of enrichment, and rather poorly by molybdenum as a consequence of the problems noted above which are attached

to obtaining accurate EDX data for this element. No particular pattern is shown for silicon, which, in any case, is more soluble in ferrite, and hence will tend to partition in the opposite direction to the other substitutional alloying elements at a rate which is not governed by the rate of diffusion in ferrite, so that equation (6.1) would not apply.

The gradient of the best fit line also shows a general trend of increasing with time. This is again in accordance with the size effect predicted by the theory behind equation (6.1): smaller particles would be expected to increase in composition more rapidly, such that the effect of particle size on composition change becomes more marked with increased ageing time. A semi-empirical illustration of this feature is given below (section 6.2.4). The t-distribution significance test on the regression analysis also generates a generally increasing level of significance to the calculated best fit gradient. This acts as further confirmation that a size effect is present. These trends are also illustrated by the plots in figure 6.1(a–e).

It can be seen from the figures that individual measured compositions are scattered around the theoretically expected composition to some degree. The distribution around \bar{c} in the as-transformed condition suggests that this is probably, at least in part, a statistical fluctuation associated with the EDX technique; it is known from theory that bainite forms with negligible substitutional redistribution, so that c_0 for the cementite particles should be very close to \bar{c} . This scatter tends to be more marked for smaller particles, where a weaker intensity of signal would lead to a higher signal to noise ratio which would exaggerate any such effect.

A comparison of compositions for earlier and later aged specimens in figure 6.1 suggests that the degree of scatter shown by individual values of c^θ for a particular ageing time is greater for longer ageing times. It should be emphasized that the simple analytical model does not account for any soft impingement, where the diffusion fields of adjacent particles overlap cause a slowing down in the rate of diffusion. Nor does the model account for irregular interparticle spacing of the type which was observed experimentally; it considers a single,

‘average’ particle with a similarly averaged ferrite region adjacent to it. In effect, to apply the model to a multi-precipitate system is to assume that both the cementite particle size and particle distribution are uniform, which is known not to be the case. In reality, more closely spaced cementite particles will be subject to soft impingement effects after a shorter ageing time than will those which are more widely spaced. It is probable that, at longer ageing times and higher temperatures where soft impingement in the ferrite becomes of significance, some of the c^θ measurements will be obtained from (more closely-spaced) particles where the effect is larger, resulting in a lower c^θ than that predicted by the model; whereas more widely-spaced particles may continue to fit the analytical model. This would add a systematic scatter to the experimental statistical scatter at longer ageing times, in keeping with the actual scatter of data which is seen in the experimental c^θ distributions (figure 6.1(a-e)).

The intercept of the best fit line with the y-axis on the $(c - \bar{c})$ versus $1/x_\theta$ plot) was also noted. This corresponds to $x_\theta = \infty$ so has no physical significance, but it can be seen intuitively that an infinitely large particle will show zero mean enrichment by diffusion of a species at a finite rate for all finite ageing times. If this intercept ceases to be at \bar{c} then it is evident that equation (6.1) no longer describes the situation entirely.

It was found that the best-fit line intercept with the y-axis was zero to within the bounds of experimental accuracy except at the longest ageing times, where a small positive value was consistently observed. It appears that $(c - \bar{c})$ ceases to be strictly proportional to x_θ^{-1} , although a marked size effect is still observed.

It is suggested that this deviation from the predictions of equation (6.1) may arise from the way that the analytical model considers the structure to be of the form of one slab of cementite, of thickness x_θ , in slabs of ferrite whose size is calculated from the lever rule, and does not include a consideration of soft impingement. It is possible that smaller cementite particles will be associated with smaller ferritic sub-units, in which case they will be more closely spaced. Thus, the onset of significant levels of soft impingement could affect the enrich-

ment of smaller cementite particles sooner than larger ones. A slowing down of the enrichment rate of the smaller particles relative to the large ones due to soft impingement would lead to a non-linearity in $(c - \bar{c})$ versus x_θ^{-1} , and a tendency for the intercept of the best fit line with $x_\theta^{-1} = 0$ to be non-zero. In any case, the onset of soft impingement means that equation (6.1) cannot rigorously be applied.

It is also possible that the problem arises in part as a consequence of particle coarsening, which the analytical model ignores, but which seemed to be occurring to a small degree from x_θ measurements. As a result of coarsening during ageing, it is not strictly correct to compare $x_\theta = 0.15\mu\text{m}$ (for instance) at zero time and large ageing time under the assumption that the data represents the same particle. It can be assumed that, where particle coarsening is taking place, enrichment of a given particle will have occurred at a more rapid rate during the early stages of ageing when the relevant cementite particle was smaller; hence, some deviation from strict proportionality in the $(c - \bar{c})$ versus x_θ^{-1} relation can be expected.

6.2.3 Mixed microstructure

The data for the approximately 30% bainitic / 70% allotriomorphic ferrite microstructure aged at 565°C are presented in table 6.4. It is immediately apparent that the cementite enrichment rate is more rapid than for the fully-bainitic case at this temperature, especially in the early stages of ageing. This can be attributed in part to the fact that the cementite particle size tends to be slightly smaller than was the case for the fully-bainitic microstructure, which equation (6.1) predicts should lead to an increased rate of enrichment. Furthermore, it can be assumed that carbon partitions into the retained austenite during formation of the allotriomorphic ferrite phase, whereas the relative proportions of substitutional alloying elements and iron remain the same; hence, the 30% bainitic region will contain almost all the carbon. This leads to a much greater carbon concentration in α_b than was the case for the fully-bainitic microstructure, and a correspondingly increased value for V_θ in this region. In order to maintain equilibrium partitioning into an increased volume fraction of cementite, it is

clear that both $c^{\alpha\theta}$ and $c^{\theta\alpha}$ will be reduced compared with the fully-bainitic case, increasing the driving force for the rate-controlling process of diffusion in the ferrite ($(\bar{c} - c^{\alpha\theta})$ in equation (6.1)) and thus reducing t_c .

Apart from the difference in enrichment rate, general trends in the data are similar to the fully-bainitic case, although the statistical scatter associated with single measurements of composition change in the mixed microstructure is generally found to be greater. This may be due to the smaller particle size: throughout the work values of $(c^\theta - \bar{c})$ appeared to be less reliable for smaller cementite particles. In consequence, despite the more rapid enrichment rate, correlation to the predicted size effect is much the same as in the case of the fully-bainitic microstructure aged at 565°C.

It can be seen intuitively, and from equation (6.1), that reducing x_θ and increasing V_θ will lead to a much reduced x_α , or inter-cementite spacing. Consequently, soft impingement can be expected to occur earlier, so that the problems associated with it (above) will become significant at relatively shorter ageing times. This may explain the fact that the correlation of the $(c - \bar{c}) \propto x_\theta^{-1}$ relationship ceases to improve (and in some cases deteriorates) at longer ageing times, and that the enrichment rate of the molybdenum in particular appears to slow at longer ageing times. Nevertheless, a general trend of improved agreement with equation (6.1) is exhibited by the data as ageing proceeds.

CHROMIUM at 510°C						
Ageing time (hours)	No of points	Mean c change (at %)	Mean x_θ μm	Data from best fit $(c - \bar{c}) \text{ v } x_\theta$		
				correlation	gradient	significance
0	31	0.06	0.161	-0.10	-0.033	<0.90
2	28	-0.02	0.149	0.11	0.022	<0.90
6	34	0.46	0.148	0.29	0.076	0.90
12	26	0.34	0.155	0.28	0.068	<0.90
24	30	0.28	0.149	-0.12	-0.032	<0.90
48	28	0.58	0.157	0.45	0.098	0.95
96	34	0.58	0.169	0.19	0.056	<0.90
168	27	0.92	0.160	0.43	0.144	0.95
336	28	1.49	0.162	0.56	0.138	0.98
672	31	1.99	0.157	0.59	0.163	0.99
1008	27	2.22	0.163	0.54	0.141	0.95
1344	32	2.23	0.169	0.57	0.149	0.98
2016	30	2.36	0.166	0.55	0.177	0.98
2688	28	2.72	0.158	0.56	0.192	0.98
4032	34	2.81	0.162	0.54	0.232	0.99
6240	27	3.89	0.171	0.61	0.283	0.99
8064	28	4.47	0.173	0.52	0.245	0.98

Table 6.1 (a) Fe–Cr–Mo power plant steel, initially with a fully-bainitic microstructure, aged at 510°C. EDX analysis data obtained for chromium content of cementite.

MANGANESE at 510°C						
Ageing time (hours)	No of points	Mean c change (at %)	Mean x_θ μm	Data from best fit $(c - \bar{c})$ v x_θ		
				correlation	gradient	significance
0	31	0.00	0.161	0.10	0.024	<0.90
2	28	0.04	0.149	-0.18	-0.025	<0.90
6	34	0.24	0.148	0.36	0.073	0.90
12	26	0.24	0.155	0.47	0.092	0.95
24	30	0.35	0.149	0.10	0.021	<0.90
48	28	0.41	0.157	0.43	0.087	0.95
96	34	0.24	0.169	0.17	0.041	<0.90
168	27	0.66	0.160	0.28	0.068	<0.90
336	28	0.58	0.162	0.42	0.042	0.90
672	31	0.78	0.157	0.46	0.062	0.95
1008	27	0.72	0.163	0.48	0.058	0.95
1344	32	0.79	0.169	0.53	0.088	0.99
2016	30	0.88	0.166	0.52	0.100	0.95
2688	28	1.00	0.158	0.37	0.114	0.90
4032	34	1.13	0.162	0.39	0.092	0.95
6240	27	1.26	0.171	0.52	0.121	0.98
8064	28	1.66	0.173	0.54	0.144	0.99

Table 6.1 (b) Fe–Cr–Mo power plant steel, initially with a fully-bainitic microstructure, aged at 510°C. EDX analysis data obtained for manganese content of cementite.

MOLYBDENUM at 510°C						
Ageing time (hours)	No of points	Mean c change (at %)	Mean x_θ μm	Data from best fit $(c - \bar{c}) \text{ v } x_\theta$		
				correlation	gradient	significance
0	31	0.42	0.161	0.00	0.001	<0.90
2	28	0.21	0.149	-0.05	-0.007	<0.90
6	34	0.54	0.148	0.34	0.101	0.95
12	26	0.55	0.155	-0.35	-0.103	0.90
24	30	0.34	0.149	-0.22	-0.061	<0.90
48	28	0.60	0.157	0.07	0.017	<0.90
96	34	0.39	0.169	0.00	0.000	<0.90
168	27	0.54	0.160	0.13	0.039	<0.90
336	28	0.35	0.162	-0.10	-0.017	<0.90
672	31	0.46	0.157	0.22	0.048	<0.90
1008	27	0.79	0.163	0.30	0.066	<0.90
1344	32	0.58	0.169	0.00	0.003	<0.90
2016	30	0.49	0.166	0.48	0.126	0.90
2688	28	0.89	0.158	0.19	0.044	<0.90
4032	34	0.67	0.162	0.29	0.055	0.90
6240	27	0.88	0.171	0.42	0.080	0.95
8064	28	1.02	0.173	0.42	0.125	0.95

Table 6.1 (c) Fe–Cr–Mo power plant steel, initially with a fully-bainitic microstructure, aged at 510°C. EDX analysis data obtained for molybdenum content of cementite.

SILICON at 510°C						
Ageing time (hours)	No of points	Mean c change (at %)	Mean x_θ μm	Data from best fit $(c - \bar{c})$ v x_θ		
				correlation	gradient	significance
0	31	-0.20	0.161	-0.21	-0.036	<0.90
2	28	-0.17	0.149	0.12	0.014	<0.90
6	34	-0.08	0.148	0.01	0.002	<0.90
12	26	-0.31	0.155	0.07	0.012	<0.90
24	30	-0.28	0.149	0.07	0.018	<0.90
48	28	-0.13	0.157	-0.07	-0.009	<0.90
96	34	-0.40	0.169	0.10	0.018	<0.90
168	27	-0.21	0.160	-0.10	-0.017	<0.90
336	28	-0.28	0.162	0.25	0.037	<0.90
672	31	-0.16	0.157	-0.24	-0.044	<0.90
1008	27	-0.23	0.163	-0.28	-0.044	<0.90
1344	32	-0.16	0.169	-0.05	-0.011	<0.90
2016	30	-0.19	0.166	-0.20	-0.020	<0.90
2688	28	-0.20	0.158	-0.38	-0.074	0.90
4032	34	-0.26	0.162	0.12	0.023	<0.90
6240	27	-0.25	0.171	-0.06	-0.009	<0.90
8064	28	-0.28	0.173	0.32	0.063	0.90

Table 6.1 (d) Fe-Cr-Mo power plant steel, initially with a fully-bainitic microstructure, aged at 510°C. EDX analysis data obtained for silicon content of cementite.

CHROMIUM at 565°C						
Ageing time (hours)	No of points	Mean c change (at %)	Mean x_θ μm	Data from best fit $(c - \bar{c}) \text{ v } x_\theta$		
				correlation	gradient	significance
0	34	0.11	0.160	-0.10	-0.021	<0.90
1	26	0.53	0.165	-0.12	-0.032	<0.90
4	29	0.54	0.149	0.11	0.019	<0.90
8	29	0.50	0.156	0.29	0.087	0.95
12	37	0.59	0.160	0.35	0.062	0.95
24	32	0.65	0.173	0.20	0.068	<0.90
48	27	1.19	0.159	0.42	0.136	0.95
96	31	1.67	0.167	0.52	0.151	0.98
168	30	1.77	0.162	0.57	0.201	0.99
336	31	1.89	0.171	0.38	0.186	0.90
672	26	3.09	0.163	0.40	0.175	0.90
1344	31	3.70	0.177	0.45	0.264	0.98
2688	29	3.53	0.170	0.47	0.247	0.95
4032	32	4.00	0.180	0.46	0.302	0.98
7002	27	4.69	0.174	0.54	0.331	0.99

Table 6.2 (a) Fe-Cr-Mo power plant steel, initially with a fully-bainitic microstructure, aged at 565°C. EDX analysis data obtained for chromium content of cementite.

MANGANESE at 565°C						
Ageing time (hours)	No of points	Mean c change (at %)	Mean x_θ μm	Data from best fit $(c - \bar{c})$ v x_θ		
				correlation	gradient	significance
0	34	0.05	0.160	-0.11	-0.024	<0.90
1	26	0.23	0.165	-0.02	-0.009	<0.90
4	29	0.33	0.149	-0.05	-0.007	<0.90
8	29	0.30	0.156	0.13	0.025	<0.90
12	37	0.33	0.160	0.28	0.037	0.90
24	32	0.41	0.173	0.48	0.152	0.98
48	27	0.74	0.159	0.29	0.133	0.90
96	31	1.06	0.167	0.42	0.080	0.95
168	30	0.86	0.162	0.58	0.118	0.99
336	31	1.37	0.171	0.28	0.172	<0.90
672	26	1.17	0.163	0.49	0.156	0.99
1344	31	1.92	0.177	0.50	0.187	0.98
2688	29	1.97	0.170	0.56	0.207	0.99
4032	32	2.41	0.180	0.38	0.149	0.95
7002	27	3.08	0.174	0.55	0.177	0.98

Table 6.2 (b) Fe–Cr–Mo power plant steel, initially with a fully-bainitic microstructure, aged at 565°C. EDX analysis data obtained for manganese content of cementite.

MOLYBDENUM at 565°C						
Ageing time (hours)	No of points	Mean c change (at %)	Mean x_θ μm	Data from best fit $(c - \bar{c}) \text{ v } x_\theta$		
				correlation	gradient	significance
0	34	0.67	0.160	-0.13	-0.036	<0.90
1	26	0.82	0.165	0.09	0.037	<0.90
4	29	0.31	0.149	0.06	0.012	<0.90
8	29	0.14	0.156	0.07	0.019	<0.90
12	37	0.49	0.160	-0.04	-0.007	<0.90
24	32	0.46	0.173	0.11	0.036	<0.90
48	27	0.31	0.159	0.13	0.046	<0.90
96	31	0.79	0.167	0.29	0.080	<0.90
168	30	0.64	0.162	0.18	0.052	<0.90
336	31	0.84	0.171	0.34	0.075	0.90
672	26	1.03	0.163	0.06	0.026	<0.90
1344	31	0.76	0.177	0.43	0.112	0.98
2688	29	1.30	0.170	-0.31	-0.075	<0.90
4032	32	0.89	0.180	0.42	0.170	0.98
7002	27	1.40	0.174	0.02	0.007	<0.90

Table 6.2 (c) Fe–Cr–Mo power plant steel, initially with a fully-bainitic microstructure, aged at 565°C. EDX analysis data obtained for molybdenum content of cementite.

SILICON at 565°C						
Ageing time (hours)	No of points	Mean c change (at %)	Mean x_θ μm	Data from best fit ($c - \bar{c}$) v x_θ		
				correlation	gradient	significance
0	34	-0.25	0.160	0.25	-0.051	<0.90
1	26	-0.33	0.165	0.02	0.004	<0.90
4	29	-0.12	0.149	0.02	0.007	<0.90
8	29	-0.44	0.156	-0.18	-0.029	<0.90
12	37	-0.09	0.160	-0.13	-0.010	<0.90
24	32	-0.06	0.173	-0.20	-0.046	<0.90
48	27	-0.39	0.164	-0.16	-0.038	<0.90
96	31	-0.16	0.167	0.01	0.002	<0.90
168	30	-0.38	0.162	-0.29	-0.058	0.90
336	31	-0.40	0.171	-0.24	-0.045	<0.90
672	26	-0.40	0.163	-0.18	-0.039	<0.90
1344	31	-0.23	0.177	-0.25	-0.064	<0.90
2688	29	-0.43	0.170	-0.23	-0.046	<0.90
4032	32	-0.22	0.180	-0.13	-0.031	<0.90
7002	27	-0.37	0.174	0.13	0.028	<0.90

Table 6.2 (d) Fe-Cr-Mo power plant steel, initially with a fully-bainitic microstructure, aged at 565°C. EDX analysis data obtained for silicon content of cementite.

CHROMIUM at 625°C						
Ageing time (hours)	No of points	Mean c change (at %)	Mean x_θ μm	Data from best fit $(c - \bar{c})$ v x_θ		
				correlation	gradient	significance
0	27	0.07	0.154	-0.05	-0.016	<0.90
1	28	0.20	0.140	0.22	0.069	<0.90
2	30	0.40	0.166	0.27	0.060	<0.90
4	32	0.89	0.156	0.35	0.082	0.90
8	29	1.37	0.152	0.48	0.124	0.98
12	32	1.88	0.161	0.40	0.154	0.95
24	25	1.76	0.155	0.56	0.215	0.98
48	31	2.86	0.176	0.57	0.258	0.99
96	30	2.95	0.162	0.54	0.293	0.98
168	28	3.30	0.181	0.46	0.298	0.95
336	32	4.57	0.183	0.62	0.319	0.99
672	29	5.78	0.176	0.59	0.348	0.99
1344	31	6.16	0.188	0.66	0.358	0.99
2688	30	6.81	0.190	0.60	0.296	0.95
4032	26	7.93	0.177	0.50	0.308	0.95
6048	29	8.69	0.186	0.48	0.382	0.98

Table 6.3 (a) Fe–Cr–Mo power plant steel, initially with a fully-bainitic microstructure, aged at 625°C. EDX analysis data obtained for chromium content of cementite.

MANGANESE at 625°C						
Ageing time (hours)	No of points	Mean c change (at %)	Mean x_θ μm	Data from best fit $(c - \bar{c})$ v x_θ		
				correlation	gradient	significance
0	27	0.03	0.154	-0.19	-0.029	<0.90
1	28	0.14	0.140	0.21	0.049	<0.90
2	30	0.17	0.166	0.29	0.031	<0.90
4	32	0.74	0.156	0.46	0.068	0.90
8	29	0.68	0.152	0.50	0.099	0.95
12	32	0.85	0.161	0.51	0.091	0.98
24	25	1.13	0.155	0.47	0.086	0.98
48	31	1.32	0.176	0.40	0.094	0.95
96	30	0.80	0.162	0.34	0.090	0.90
168	28	1.70	0.181	0.23	0.068	<0.90
336	32	1.49	0.183	0.48	0.107	0.98
672	29	1.76	0.176	0.58	0.178	0.99
1344	31	2.23	0.188	0.41	0.095	0.95
2688	30	2.72	0.190	0.52	0.167	0.98
4032	26	3.41	0.177	0.51	0.190	0.99
6048	29	3.45	0.186	0.37	0.164	0.95

Table 6.3 (b) Fe–Cr–Mo power plant steel, initially with a fully-bainitic microstructure, aged at 625°C. EDX analysis data obtained for manganese content of cementite.

MOLYBDENUM at 625°C						
Ageing time (hours)	No of points	Mean c change (at %)	Mean x_θ μm	Data from best fit $(c - \bar{c}) \text{ v } x_\theta$		
				correlation	gradient	significance
0	27	0.42	0.154	-0.22	-0.070	<0.90
1	28	0.64	0.140	0.06	0.024	<0.90
2	30	0.41	0.146	-0.36	-0.155	<0.90
4	32	0.73	0.156	0.32	0.040	<0.90
8	29	0.29	0.152	-0.04	-0.007	<0.90
12	32	0.95	0.161	0.13	0.017	<0.90
24	25	0.58	0.155	0.20	0.047	<0.90
48	31	0.83	0.176	0.10	0.025	<0.90
96	30	0.41	0.162	-0.19	-0.043	<0.90
168	28	0.91	0.181	0.33	0.084	0.90
336	32	1.07	0.183	0.35	0.078	0.90
672	29	0.53	0.176	0.35	0.096	0.90
1344	31	0.89	0.188	0.43	0.115	0.95
2688	30	1.19	0.190	0.62	0.216	0.99
4032	26	1.02	0.177	0.10	0.035	<0.90
6048	29	1.60	0.186	0.39	0.005	<0.90

Table 6.3 (c) Fe–Cr–Mo power plant steel, initially with a fully-bainitic microstructure, aged at 625°C. EDX analysis data obtained for molybdenum content of cementite.

SILICON at 625°C						
Ageing time (hours)	No of points	Mean c change (at %)	Mean x_θ μm	Data from best fit $(c - \bar{c}) \text{ v } x_\theta$		
				correlation	gradient	significance
0	27	-0.20	0.154	0.09	0.019	<0.90
1	28	-0.38	0.140	-0.13	-0.019	<0.90
2	30	-0.11	0.166	0.11	0.018	<0.90
4	32	-0.35	0.156	0.20	0.025	<0.90
8	29	-0.26	0.152	0.16	0.025	<0.90
12	32	-0.21	0.161	-0.18	-0.027	<0.90
24	25	-0.38	0.155	-0.25	-0.033	<0.90
48	31	-0.26	0.176	0.16	0.029	<0.90
96	30	-0.38	0.162	-0.39	-0.074	0.90
168	28	-0.26	0.181	0.13	0.020	<0.90
336	32	-0.30	0.183	-0.03	-0.004	<0.90
672	29	-0.26	0.176	-0.07	-0.010	<0.90
1344	31	-0.38	0.188	-0.36	-0.080	0.90
2688	30	-0.27	0.190	-0.30	-0.040	<0.90
4032	26	-0.39	0.177	0.26	0.052	<0.90
6048	29	-0.14	0.186	-0.03	-0.007	<0.90

Table 6.3 (d) Fe-Cr-Mo power plant steel, initially with a fully-bainitic microstructure, aged at 625°C. EDX analysis data obtained for silicon content of cementite.

CHROMIUM at 565°C						
Ageing time (hours)	No of points	Mean c change (at %)	Mean x_θ μm	Data from best fit $(c - \bar{c})$ v x_θ		
				correlation	gradient	significance
0	29	0.15	0.150	-0.02	-0.040	<0.90
1	26	0.49	0.146	0.31	0.052	<0.90
2	27	0.35	0.140	0.03	0.006	<0.90
4	32	0.82	0.143	0.13	0.027	<0.90
12	32	0.87	0.150	0.38	0.077	0.95
24	28	1.30	0.164	0.25	0.082	<0.90
48	28	1.97	0.145	0.61	0.214	0.99
96	31	2.73	0.152	0.61	0.260	0.99
168	27	3.54	0.152	0.59	0.296	0.99
336	27	4.37	0.135	0.47	0.350	0.98
672	29	4.46	0.150	0.28	0.210	<0.90
1344	31	4.82	0.157	0.62	0.447	0.99
2688	26	5.79	0.152	0.51	0.357	0.98
5376	31	6.53	0.156	0.43	0.443	0.95

Table 6.4 (a) Fe–Cr–Mo power plant steel, initially with a mixed ferritic and bainitic microstructure, aged at 565°C. EDX analysis data obtained for chromium content of cementite.

MANGANESE at 565°C						
Ageing time (hours)	No of points	Mean c change (at %)	Mean x_θ μ m	Data from best fit ($c - \bar{c}$) v x_θ		
				correlation	gradient	significance
0	29	0.03	0.150	-0.21	-0.039	<0.90
1	26	0.41	0.146	0.07	0.007	<0.90
2	27	0.32	0.140	0.14	0.014	<0.90
4	32	0.32	0.143	0.05	0.004	<0.90
12	32	0.40	0.150	0.40	0.044	0.95
24	28	0.95	0.164	0.30	0.057	<0.90
48	28	0.89	0.145	0.67	0.149	0.95
96	31	0.98	0.152	0.48	0.108	0.95
168	27	1.20	0.152	0.61	0.163	0.99
336	27	2.18	0.135	0.40	0.083	0.90
672	29	2.71	0.150	0.22	0.086	<0.90
1344	31	2.56	0.157	0.49	0.196	0.98
2688	26	2.60	0.152	0.34	0.200	0.90
5376	31	3.75	0.156	0.60	0.151	0.99

Table 6.4 (b) Fe–Cr–Mo power plant steel, initially with a mixed ferritic and bainitic microstructure, aged at 565°C. EDX analysis data obtained for manganese content of cementite.